PHILLIPS LABORATORY SCHOLAR PROGRAM

Janette D. Peele
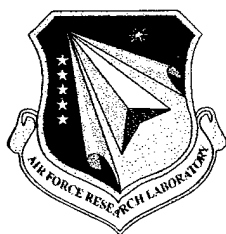
Northeast Consortium for Engineering Education
68 Port Royal Square
Port Royal, VA 22535

May 1998

Final Report
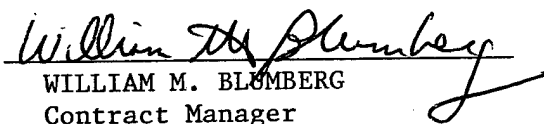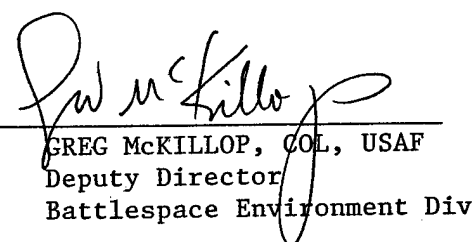
20020619 006

AIR FORCE RESEARCH LABORATORY
Space Vehicles Directorate
29 Randolph Road
AIR FORCE MATERIEL COMMAND
HANSCOM AIR FORCE BASE MA 01731-3010

"This technical report has been reviewed and is approved for publication"

WILLIAM M. BLUMBERG
Contract Manager

GREG McKILLOP, COL, USAF
Deputy Director
Battlespace Environment Div

REPORT DOCUMENTATION PAGE

Form Approved
OMB No. 0704-0188

1. REPORT DATE (DD-MM-YYYY)	2. REPORT TYPE	3. DATES COVERED (From - To)
28 May 1998	Final	28May93–28May98

4. TITLE AND SUBTITLE	5a. CONTRACT NUMBER
Phillips Laboratory Scholar Program Management & Technical Report	F19628-93-C-0027

5b. GRANT NUMBER

5c. PROGRAM ELEMENT NUMBER
62101F

6. AUTHOR(S)	5d. PROJECT NUMBER
Janette D. Peele, Program Director	9993

5e. TASK NUMBER
GS

5f. WORK UNIT NUMBER
PR

7. PERFORMING ORGANIZATION NAME(S) AND ADDRESS(ES)	8. PERFORMING ORGANIZATION REPORT NUMBER
Northeast Consortium for Engineering Education 68 Port Royal Square Port Royal, VA 22535	

9. SPONSORING / MONITORING AGENCY NAME(S) AND ADDRESS(ES)	10. SPONSOR/MONITOR'S ACRONYM(S)
Air Force Research Laboratory/VSB 29 Randolph Road Hanscom AFB MA 01731-3010	

11. SPONSOR/MONITOR'S REPORT NUMBER(S)
AFRL-VS-TR-2002-1559

12. DISTRIBUTION / AVAILABILITY STATEMENT

Approved for public release: distribution unlimited

13. SUPPLEMENTARY NOTES

14. ABSTRACT
The USAF Phillips Laboratory Scholar Program provided research opportunities for qualified doctorate-level engineers and scientists to work in the laboratory either at Hanscom Air Force Base, Mass., or at Kirtland Air Force Base, N.M. Twenty-seven scholars participated during the period of the contract, including four during the period 1 July 1997-28 May 1998. Dr. Sean Carey used UV extinction data to investigate the properties of interstellar dust grains and used data from the Midcourse Space Experiment (MSX) to investigate the structure of infrared-dark clouds. Dr. Brian Kane used data from the Five Colleges Radio Astronomy Observatory and the Infrared Space Observatory (ISO) to investigate the structure and kinematics of Bok globules, which are small, isolated, star-forming clouds in our galaxy. Dr. Anthony Midey measured rate constants for ion-molecule reactions, using a high-temperature flowing afterglow (HTFA) apparatus. Dr. Susan Triantafillou adapted the lattice Boltzmann (LB) computational method to the prediction of atmospheric phenomena, including cloud development and turbulent eddies. Results of these research efforts are described in the individual contributions of the Scholars to this final report.

15. SUBJECT TERMS

Phillips Laboratory Scholar Program, Interstellar dust grains, Mid-infrared dark clouds, Bok globules, High temperature flowing afterglow, Lattice Boltzmann model

16. SECURITY CLASSIFICATION OF:			17. LIMITATION OF ABSTRACT	18. NUMBER OF PAGES	19a. NAME OF RESPONSIBLE PERSON
a. REPORT	b. ABSTRACT	c. THIS PAGE			William A.M. Blumberg
Unclassified	Unclassified	Unclassified	Unlimited	48	19b. TELEPHONE NUMBER (include area code) 781-377-3601

Standard Form 298 (Rev. 8-98)
Prescribed by ANSI Std. Z39.18

INTRODUCTION

The USAF Phillips Laboratory Scholar Program is sponsored by the Phillips Laboratory Geophysics Directorate. It is conducted by the Northeast Consortium for Engineering Education (NCEE). This program provides research opportunities for qualified engineers and scientists who have received their PhD degrees, or equivalent, from technical programs at U.S. universities or technical institutions. These opportunities consist of research appointments of 12 months duration with the Geophysics Directorate, located at Hanscom AFB near Boston, Massachusetts, or the Advanced Weapons and Survivability Directorate located at Kirtland Air Force Base, New Mexico.

PROGRAM DESCRIPTION

The Air Force Geophysics Directorate has initiated the Phillips Laboratory Scholar Program to broaden the direct participation of qualified researchers in Phillips Laboratory research programs. This program has provided research opportunities for selected engineers and scientists holding a doctoral degree to work at the Air Force Phillips Laboratory for a 12 month research period; the appointment may be extended for a second term.

To be eligible, candidates must have a PhD or equivalent experience in an appropriate technical field. Scholars located at Hanscom AFB will be selected primarily from such basic and applied science fields as physics, particularly geophysics and atmospheric physics, chemistry computer science, and engineering. Scholars located at Kirtland AFB will be involved in pulsed power, high-density and high-energy plasmas, high-power microwave sources, electromagnetic applications and effects, satellite survivability and vulnerability analysis, and related experimental, theoretical, and computational method topics. Applicants must be U.S. citizens who are recent recipients of the PhD (within the last five years).

NCEE supports equal opportunity/affirmative action. All qualified applicants will receive consideration without regard to race, color, religion, sex, or national origin.

PROGRAM OBJECTIVES

(1) To provide a productive means for scientists and engineers holding PhD degrees to participate in research at the Air Force Phillips Laboratory;

(2) To stimulate continuing professional association among the Scholars and their professional peers in the Air Force;

(3) To further the research objectives of the United States Air Force;

(4) To enhance the research productivity and capabilities of scientists and engineers especially as these relate to Air Force technical interests.

This report covers the period 1 July 1997 through 28 May 1998. Four scholars participated in the Phillips Laboratory Scholar Program during this period with two completing the program.

UNITED STATES AIR FORCE

PHILLIPS LABORATORY SCHOLAR PROGRAM

conducted by the

NORTHEAST CONSORTIUM FOR ENGINEERING EDUCATION

FINAL REPORT

Prepared by: Dr. Sean J. Carey.

Research Location: Phillips Laboratory,
                                        Hanscom AFB, MA   01731

Contract Number: F19628-93-C-0027

<u>Geophysics Scholar Final Report</u>

Sean J. Carey

My tenure as a Geophysics Scholar began July 15, 1997 and ends April 21, 1998. During this time, I have worked on two separate projects, an investigation of grain destruction around mid to late B stars and the discovery and investigation of the MSX mid-infrared dark clouds. This final report contains three sections. The first two sections discuss my two projects with a brief introduction, a summary of important results and a short description of the work completed. The final section of the report lists the papers published, presentations given, and meetings attended during my tenure.

Grain Destruction Around B Stars:

Work is in collaboration with Drs. Frank O. Clark and Russell F. Shipman of VSBC/AFRL and Dr. Rob Assendorp of the Astrophysikalishches Institut Potsdam.

The exact nature of the composition and size distribution of interstellar dust grains is a current and very important area of research. Interstellar dust grains are 10 Å to 1 µm sized solids composed of silicate and carbonaceous compounds. The properties of interstellar dust grains are inferred from the visible and UV starlight they absorb and scatter (the combination of absorption and scattering is called extinction) and re-radiate in the infrared. We investigated the infrared emission and ultraviolet extinction of interstellar dust in which main sequence B stars are embedded to determine how the enhanced radiation field near the star affects the interstellar dust. In particular, we studied the properties of the smallest dust grains (< 0.1 µm), as they are the most affected by the presence of an enhanced radiation field. The smallest dust grains are heated stochastically by UV photons and emit primarily at wavelengths of 12-25 µm. In addition, the UV extinction is more sensitive to variations in the number and physical properties of these smaller dust grains.

Our study was motivated by previous work of Shipman (1995) and Shipman & Clark (1995) who studied dust emission in HII regions. They determined that 12 and 25 µm (small grain) emission declined relative to the emission at 100 µm (due primarily to larger grains) as the radiation field increased. They interpret the relative decline in 12 and 25 µm emission to the destruction of small grains by the high flux of UV photons from the exciting star of the HII region. We extend this prior work by studying the lower UV flux regions around B stars. Specifically, we are interested in determining the hardness of the radiation field necessary to produce 12 and 25 µm emission deficits and using the results to determine the structure of the small grains. Our preliminary investigation (Carey *et al.* 1997) determined that the 12 and 25 µm emission was deficient in the region around B stars.

Methodology:
The sample set of stars studied was taken from the list of stars embedded in infrared cirrus clouds complied by Gaustad & Van Buren (1993). From this list, we selected bright, main sequence stars of spectral types B1.5-B9 within 1000 parsecs. The IRAS ISSA images (Wheelock *et al.* 1994) at 12, 25, 60 and 100 µm were examined for emission around each star. We restricted our sample set to the 20 stars with the least confused infrared backgrounds. The infrared emission was averaged in annuli around each star to construct an emission profile as a function of angular distance from

the star at 12, 25, 60 and 100 μm. A background was subtracted from each annulus to account for foreground emission and the uncertainty in the DC offset level of the ISSA images. Detector hysteresis and AC/DC responsivity variations were investigated and determined not to affect the quality of the data. Color ratios were calculated from the averaged emission profiles. The color ratio profiles were compared with the grain emission models of Desert, Boulanger and Puget (DBP; 1990). The model results were converted to angular distance from the star and ratioed to produce color profiles for comparison.

We measured the UV extinction toward four of the stars using UV photometry from the Astronomical Netherlands Satellite. We used the UV color excesses published by Savage et al. (1985). We fit the observed extinction curves with the model of Clayton, Cardelli and Mathis to derive the ratio of selective-to-total extinction (R_v) for the lines of sight towards the stars studied.

Results:
For all sources, the infrared emission at 12, 25, 60 and 100 μm increases as the star is approached. The 60/100 color is well modeled by DBP rising from a uniform background value of 0.2 to a peak at the position of the star. Surprisingly, the rise in 25 μm emission begins at a larger distance from the star than the 60 μm increase. It appears that the 25 μm emitters are more responsive than the rest of the grains to slight changes in the radiation field. Five stars have declining 12/100 and 25/100 colors as the star is approached, which is in direct conflict with the DBP model. The 25/100 decline is more pronounced than the 12/100 decline. The 12/100 and 25/100 color deficits are associated with far-UV extinctions lower than the standard interstellar value. Destruction of small grains in the increased radiation field near the star is necessary to explain the correspondence of 12/100 and 25/100 color deficits with low far-UV extinction. The particulars of the color variation imply that the 25 μm emitters are preferentially destroyed. Our investigation suggests that the carriers of the 25 μm emission are loosely bonded aggregates of carbonaceous compounds such as polycyclic aromatic hydrocarbons. These aggregates can be photodissociated by the moderate enhancement in the ultraviolet radiation field found around main sequence B stars. Our analysis is consistent with the conglomerate grain model of Clark et al. (1995).

References:
Clayton, G. C., Cardelli, J. A., & Mathis, J. S. 1988, ApJ, 329, L33
Carey, S. J., Shipman, R. F., Clark, F. O., & Assendorp, R. 1997, ApJ, 479, 303
Clark, F. O., Shipman, R. F., Assendorp, R., Kester, D., & Egan, M. P. 1995, Plan. Sp. Sci., 43, 1353
Désert, F.-X., Boulanger, F., & Puget J. L. 1990, A&A, 237, 215
Gaustad, J. E., & van Buren, D. 1993, PASP, 105, 1127
Savage, B. D., Massa, D., Meade, M., Wesselius, P. 1985, ApJS, 59, 397
Shipman, R. F. 1994, PhD. Thesis, University of Wyoming
Shipman, R. F., & Clark, F. O. 1994, ApJ, 422, 153
Wheelock, S. L. et al. 1994, IRAS Sky Survey Atlas Explanatory Supplement (JPL Publ. 94-11; Pasadena: JPL)

MSX Infrared-Dark Clouds:

Work is in collaboration with Drs. Michael P. Egan, Frank O. Clark, Stephan D. Price, Russell F. Shipman of VSBC/AFRL and Thomas A. Kuchar of Dynamic Research Corporation

The SPIRIT III infrared telescope aboard the Midcourse Space Experiment (MSX) observed the Galactic plane with high spatial resolution (18") and sensitivity in five wavelength bands between 4 and 25 μm (Price 1995). Quite surprisingly, the bright mid-infrared emission of the Galactic plane is punctuated by dark patches. These dark regions are objects foreground to the majority of the emission with high mid-infrared opacities. Motivated by the discovery of approximately 2000 of these clouds in a cursory inspection of initially processed images of the Galactic plane, we have initiated a multi-wavelength study of these infrared-dark regions (hereafter called MSX dark clouds) to better understand their physical properties.

Methodology:
One of the goals of the MSX Galactic plane survey is to produce well calibrated images of the Galactic plane in wavelength bands: 6.8-10.8 (A), 4.22-4.36 (B1), 4.24-4.45 (B2), 11.1-13.2 (C), 13.5-15.9 (D) and 18.2-25.1 (E) μm. To achieve this result, a number of data artifacts and calibration issues must be handled. Accurate calibration of the MSX data is needed to calculate the mid-infrared extinction across the MSX dark clouds. A crucial task is the proper subtraction of the instrumental dark current. The initial dark current correction provided is not sufficient for astronomical purposes. I have been involved in attempts to produce better corrections by modeling the measured dark current measurements in more detail. This work is ongoing, but initial results show that it is feasible to more accurately model the temporal variations of the dark current.

In addition to a more detailed study of the mid-infrared data, the MSX dark clouds have been observed in millimeter-wave rotational transitions of H_2CO. H_2CO is a tracer of the dense molecular gas that should be associated with the large column of dust producing the observed mid-IR extinction. We observed ten clouds using the NRAO 12 Meter telescope at Kitt Peak, Arizona. Where possible, we have mapped the MSX dark clouds in the $2_{12}-1_{11}$ line of H_2CO. By observing several different transitions of ortho and para-H_2CO and the isotopic substitutions, $H_2^{13}CO$ and HDCO, we have probed the gas density, kinetic temperature, column density and H_2CO abundance of these clouds. Line properties have been determined by the fitting of Gaussian profiles and/or direct calculation of line moments. The observed transitions have been modeled using a large velocity gradient (LVG) statistical equilibrium code (Mangum & Wootten 1993). Distances to some of the clouds have been determined from the kinematic information provided by the observed lines and a model of the Galactic rotation curve (Clemens 1985).

The far-infrared emission of the MSX dark clouds has been studied using the IRAS ISSA plates (Wheelock et al. 1994), IRAS Galaxy Atlas (Cao et al. 1997) and IRAS Groningen GEISHA high resolution images (Assendorp et al. 1995). We could not attribute far-infrared emission above the local background (1000 MJy/sr) to any of the clouds observed in H_2CO. An upper limit to the dust temperature for the clouds was set by modeling the expected emission using grain absorption coefficients from Mathis & Whiffen (1989) and assuming that the emission was due to an optical thin column of 0.1 μm sized grains. We have proposed submillimeter continuum observations using the SCUBA camera on the James Clerk Maxwell Telescope to search the clouds for

embedded protostellar objects and to definitively determine the column density and temperature of the interstellar dust in these clouds.

Results:
All ten clouds observed in H_2CO $2_{12}-1_{11}$ were detected, confirming that the MSX dark clouds contain dense molecular gas. The morphologies of the spectral line emission vary from globule shaped to filamentary and closely follow the mid-infrared extinction. We determined distances between 1.0 to 8.5 kiloparsecs to the clouds. Also, the clouds are kinematically associated with HII regions (Kuchar & Clark 1997) suggesting that they are associated with star forming regions. The linear diameters of the MSX dark clouds are 0.2-10 parsecs. The molecular column densities are between 10^{23} and 10^{25} cm^{-2} with estimates from mid-infrared extinction and H_2CO emission agreeing.

From LVG modeling, we estimate that the gas densities of the clouds are of order 10^6 cm^{-3} and the gas kinetic temperatures are 10-15 K. The upper limit to the dust temperature from the lack of far-infrared emission is 25 K. The gas and dust temperatures should be equilibrated at the densities of the MSX dark clouds. The abundance of H_2CO relative to H_2 is ~1.0 x 10^{-10} and is significantly depleted compared to more diffuse molecular clouds. It is likely that H_2CO is depleted by accretion of gas-phase metals onto the dust grains in the cold, dense MSX dark clouds.

The MSX dark clouds have nearby star-forming regions but do not have any known star-forming tracers (HII regions, masers or IR point sources) within their boundaries. Given the high densities of these objects, it is unlikely that they are stable against collapse and subsequent star formation despite the lack of star formation tracers. Indeed, the observed molecular line profiles have pronounced wings, which suggest some sort of internal motions in these clouds. It is likely that the MSX dark clouds contain internal structure in a pre-protostellar state and may contain class 0 protostars. Further observations (particularly in the submillimeter) will be able to more accurately characterize the star-forming properties of these objects.

The MSX Galactic plane survey has identified a new population of objects. These objects are extremely large, cold, dense molecular cores associated with star forming regions, but clearly in a protostellar or pre-protostellar state themselves. Further study of these exciting objects should provide crucial information to understanding the earliest stages of the star formation process.

References:
Assendorp, R., Bontekoe, T. R., de Jonge, A. R. W., Kester, D. J. M., Roelfsema, P. R., & Wesselius, P. R. 1995, A&AS, 110, 395
Cao, Y., Terebey, S., Prince, T. A., & Beichman, C. A. 1997, ApJS, 71, 89
Clemens, D. P. 1985, ApJ, 295, 422
Kuchar, T. A., & Clark, F. O. 1997, ApJ, 488, 224
Mangum, J. G., & Wootten, A. 1993, ApJS, 89, 123
Mathis, J. S., & Whiffen, G. 1989, ApJ, 341, 808
Price, S. D. 1995, Space Sci. Rev., 74, 81
Wheelock, S. L. et al. 1994, IRAS Sky Survey Atlas Explanatory Supplement (JPL Publ. 94-11; Pasadena: JPL)

Papers, Presentations and Travel During Tenure:

Papers:

Egan, M. P., Shipman, R. F., Price, S. D., Carey, S. J., Clark, F. O., & Cohen, M. 1998, "A Population of Cold Cores in the Galactic Plane", Astrophysical Journal, 194, L199

Carey, Sean J., Clark, F. O., Egan, M. P., Price, S. D., Shipman, R. F., & Kuchar, T. A. "The Physical Properties of the MSX Galactic Infrared-Dark Clouds", submitted to the Astrophysical Journal

Carey, Sean J., Shipman, R. F., & Clark, F. O., "Deficits of 25 μm Carriers Around B Stars", in preparation

Presentation given:

S. J. Carey, S. D. Price, M. P. Egan, R. F. Shipman, T. Kuchar, F. O. Clark, M. Cohen 1998, "Infrared Dark Clouds in the Milky Way", poster presented at the 191st meeting of the American Astronomical Society, Washington, DC

Proposals submitted:

"Molecular Search for MSX Dark Clouds", proposal for NRAO 12 meter observing time, observations conducted November 1-6, 1997

NRAO 12 meter unassigned time request for January 1998, observations conducted January 12, 1998

NRAO 12 meter unassigned time request for March 1998, observations conducted March 27, 1998

"Study of Physical Properties of MSX Dark Clouds", proposal for NRAO 12 meter observing time, awarded time May 16-20, 1998

"SCUBA survey of MSX Infrared-Dark Clouds", proposal for James Clerk Maxwell Telescope observing time, submitted

"Investigation of Dust Chemistry in Cold Molecular Cores", proposal for NRAO 12 meter observing time, submitted

Travel:

Observed at the NRAO 12 meter telescope, Kitt Peak, Arizona, November 1-6, 1997

Attended 191st meeting of the American Astronomical Society, Washington, DC, January 6-10, 1998

UNITED STATES AIR FORCE

PHILLIPS LABORATORY SCHOLAR PROGRAM

conducted by the

NORTHEAST CONSORTIUM FOR ENGINEERING EDUCATION

FINAL REPORT

Prepared by: Dr. Brian D. Kane.

Research Location: Phillips Laboratory,
                                    Hanscom AFB, MA 01731

Contract Number: F19628-93-C-0027

AIR FORCE RESEARCH LABS GEOPHYSICS SCHOLAR
FINAL REPORT: CONTRACT F19628-93-C-0027
Dr. Brian D. Kane

December 1995 – December 1997

INTRODUCTION

I describe in this document the summary of accomplishments during my two-year tenure as a NCEE Geophysics Scholar contracting at Air Force Research Laboratories (formerly Phillips Laboratory), Hanscom AFB, Massachusetts. I describe the work done which led to submission of papers for refereed publication, and I outline the results of my attendance at professional conferences during my tenure as a Geophysics Scholar.

WORK SUBMITTED FOR PUBLICATION

1. I researched the kinematics of small, isolated, structurally simple star-forming clouds in our Galaxy called "Bok globules." Fifteen small Bok globules showing no signs of current star formation were mapped at high spatial and especially spectral resolution in the ($J = 1 \rightarrow 0$) rotational lines of CO, ^{13}CO, and $C^{18}O$, using the 14 meter radio telescope of the Five College Radio Astronomy Observatory. Maps were made with the fifteen-element 3 mm array receiver QUARRY and the 15×1024 channel autocorrelator spectrometer FAAS. From 120 to 360 positions per globule, sampled with half-beam spacing, were observed in the ^{13}CO line, while 30 to 60 full-beam-sampled $C^{18}O$ and CO positions per globule were observed. ^{13}CO and $C^{18}O$ were observed with a velocity resolution of less than 0.007 km s^{-1} channel^{-1}; CO was observed with 0.013 km s^{-1} channel^{-1} resolution.

Gaussian fitting of the emission lines was used to establish mean radial velocities and uncertainties. Each globule radial velocity distribution on the sky was fit to a plane (solid body rotation) to yield mean velocity gradients with position, and rotation axis directions. The globules were found to be rotating at rates more than an order of magnitude faster than velocity shifts attributable to local differential Galactic rotation. For globule assumed mean distances of 600 pc, the gradients range from 0.089 km s^{-1} pc^{-1} ($\omega \sim 3 \times 10^{-15}$ s^{-1}) to

$0.950 \, \text{km s}^{-1} \, \text{pc}^{-1}$ ($\omega \sim 3 \times 10^{-14} \, \text{s}^{-1}$). Half show gradients less than about $0.3 \, \text{km s}^{-1} \, \text{pc}^{-1}$, and half show gradients greater than about $0.6 \, \text{km s}^{-1} \, \text{pc}^{-1}$, distributed in a *distinctly bimodal fashion.*

Detailed examination of the globule rotation curves indicated that the kinematics of ten of fifteen globule cores are well-approximated by solid-body rotation. Differential rotation and shearing motions due to external influences (ram pressure stripping and/or bow shocks) are also seen.

2. I researched the stellar content of some of the Bok Globules described in item 1 (and of others). Using the Infrared Space Observatory (ISO), we took ISOCAM images at 6 microns and 15 microns wavelength, in order to confirm previous implications from Infrared Astronomy Satellite (IRAS) data that said globules were star-free. ISO images provided much more sensitivity with which to make that declaration. Of the dozen or so globules studied for this paper, all but one were decided to be definitively star-free. The remaining cloud will need further study to determine its characteristics.

3. I researched the magnetic field configurations around the same Bok globules described in item 1. Fifteen small Bok globules were probed using a CCD imaging polarimeter in order to create detailed maps of the magnetic fields associated with these clouds. Stars as faint as 20th mag at V-band were measured polarimetrically with uncertainties less than 1%. Sky transmission variations were minimized via a system of synchronous polaroid rotation and bidirectional charge shifting. In all, more than 1000 stars behind the periphery of these globules were accurately analyzed polarimetrically. The large-scale (1 – 2 pc) magnetic field patterns around the SBGs may be classified into four types: Type I, two narrowly dispersed patterns which overlap spatially; Type II, one widely dispersed pattern and one narrowly dispersed pattern which overlap spatially; Type III, primarily uniform; and Type IV, cometary (polarization vectors appear to wrap around the globule). Multiple Gaussian fitting of the polarization position angle histograms results in 1σ dispersions which average around $10°$, indicating one or more predominantly uniform field directions along the line of sight. The widely dispersed primary peaks of patterns of Type II and IV are likely due to changes in the line-of-sight field direction, as evidenced

by the smooth changes in position angles with polarization. The secondary peaks of patterns of Types I, II, and III are typically produced by highly polarized, faint background stars; likely the secondary peaks trace magnetic field conditions which are not local to the SBGs.

Among the radial distributions of SBG mean polarization and position angle, there is no overall trend. However, SBGs with patterns of Type II or III tend to have stars with higher mean polarizations nearer to their centers, usually within 1' to 4'. Among the corresponding distributions of eight 45° azimuth sectors around each SBG, most of the distributions indicate two or more distinct zones of polarizations and position angles. Such zones are most distinct around SBGs with field patterns of Types II and III. The different zones likely represent regions with different line-of-sight field directions, or regions with magnetic fields tangled to different extents. This phenomenon is best seen in plots of mean polarization versus dispersions of position angles in the azimuthal sectors around each globule. Almost always, regions of high mean polarization correspond to regions of low dispersion in position angle, and vice versa.

Finally, by plotting stellar separations against differences of polarization position angles, the typical SBG was found to have a magnetic field structure function with local maxima at separations of several arcminutes (several tenths of a parsec: the mean diameter of SBGs in the sample) and of several tenths of an arcminute (several hundredths of a parsec: a possible preferred clump size in SBG cores).

4. I helped produce a high-resolution catalog of our Galactic plane, at wavelengths of 12 and 25 microns. We used a maximum entropy method to improve resolution on Infrared Astronomy Satellite (IRAS) data, and Cramer-Rao bound techniques to determine noise characteristics and accurate fluxes. Previous catalogs using IRAS data have avoided the Galactic plane (from ten degrees declination on either side, and out to 100 degrees from the Galactic center), because the many sources in this region led to confusion effects and indeterminate fluxes. This work, combined with the similar work of other groups at 60 and 100 micron wavelengths, will provide valuable spectral information for a variety of Galactic and extragalactic sources, ranging from stars to nebulae. Over 200,000 high-reliability sources were catalogued in one wavelength band or the other, or in both bands. Reliability was good

down below 0.2 Janskys in flux.

5. I researched the density structures of the same Bok globules described in items 1 and 3. Fifteen small Bok Globules were observed in the ($J = 1 \rightarrow 0$) rotational lines of CO, ^{13}CO, and $C^{18}O$, using the 14 meter radio telescope of the Five College Radio Astronomy Observatory (FCRAO). Maps were made with the fifteen-element QUARRY 3 mm array receiver and the 1024 channel FAAS autocorrelator spectrometer. A total of 120 to 360 positions per globule, sampled with half-beam spacing, was observed in the ^{13}CO line, mostly over 2.5 by 3 arcmin grids, while 30 to 60 full-beam-sampled $C^{18}O$ and CO positions per globule were observed. ^{13}CO and $C^{18}O$ were observed with a velocity resolution of less than 0.007 $km\,s^{-1}$ channel^{-1}; CO was observed with 0.013 $km\,s^{-1}$ channel^{-1} resolution.

The median SBG in the sample has an apparent volume density profile which falls off as $\sim r^{-2.6}$, significantly steeper than found in Yun & Clemens' 1991 sample (of which the majority contained YSO candidates) whose mean dust density profile fell off as a much shallower $\sim r^{-1.6}$.

Overall, assuming a distance of 600 pc, the sample of SBGs is characterized as containing cores of size 0.3 pc. SBGs contain about $10 M_\odot$ of gas, have mean H_2 densities of a few $\times 10^3$ cm^{-3}, and kinetic temperatures of $\sim$ 10 K. Most SBGs are near virial equilibrium. Using energy balance arguments, half of the SBGs may be quasi-statically contracting, and all of these globules still possess envelopes. The strongest association with cloud contraction is the existence of a relatively large envelope. Rotation is in most cases the least significant source of support against gravitational contraction; in the majority of cases kinetic energy owing to turbulent motions is providing the most support against contraction.

6. I initiated PDSL work to develop a web site devoted to astronomy and space science and technology education.

Summary: Please see the URL http://spdcc.com/kane/resume.html

CONFERENCES ATTENDED

1. My tenure at the Air Force Research Laboratories commenced with the publication of a paper given at the "Polarimetry of the Interstellar Medium" conference in Troy, NY, shortly before I began in my position. This conference was devoted both to the advancement of polarization theories and to the dissemination of the latest results in polarization studies of the space between stars which is known to form new stars. My paper was one of the latter observational studies. Revisions ensued, leading to the appearance of my paper "Investigating Correlations in the Kinematics and Magnetic Fields of Quiescent Bok Globules" in ASP Conference Series Vol. 97, ed. W. G. Roberge & D. C. B. Whittet (San Francisco: ASP), p. 269 (1996).

2. In October, 1996, I attended the Seventh Astrophysics Conference at the University of Maryland, College Park. This conference was conceived to invite discussion on the current state of star formation theories and the data currently available to confirm or rule out such theories. As such, it was a more general conference than the Polarimetry conference. I gave the paper "Rotation of Starless Bok Globules," as a prelude to my published work. This paper can be found in AIP Conference Series, Vol. 393, ed. S. H. Holt & L. G. Mundy (Woodbury, NY: AIP), p. 137 (1997).

3. In January, 1997, I attended the 189th meeting of the American Astronomical Society, held in Toronto, Ontario, Canada. I presented at work entitled "The Kinematics, Stuctures, and Magnetic Natures of Starless Bok Globules", which summarized my Ph. D. dissertation and the continuing work I had done as a Geophysics scholar to improve upon it.

4. In January, 1998, I will attend the 191st meeting of the American Astronomical Society, held in Washington, DC. I will present a paper entitled "Density Structures of Starless Bok Globules," which will be a detailed look at research commenced for my Ph. D. dissertation and which was the last project I had worked on as a Geophysics Scholar.

UNITED STATES AIR FORCE

PHILLIPS LABORATORY SCHOLAR PROGRAM

conducted by the

NORTHEAST CONSORTIUM FOR ENGINEERING EDUCATION

FINAL REPORT

Prepared by: Dr. Anthony J. Midey, Jr.

Research Location: Phillips Laboratory,
                                       Hanscom AFB, MA   01731

Contract Number: F19628-93-C-0027

Final Report

Anthony J. Midey, Jr.

NCEE Contract Period from 1 September 1997 to 27 May 1998

During the aforementioned contract period, I have utilized a high temperature flowing afterglow (HTFA) to measure rate constants for ion-molecules reactions at high temperatures under the direction of Dr. Albert A. Viggiano at the Air Force Research Laboratory in the Space Vehicles Directorate (VSBP) at Hanscom AFB, MA. Plasma chemistry occurs at very high temperatures and has a critical impact on Air Force systems. A plasma develops around re-entry vehicles that can interfere with communications. In addition, the chemistry of the ionosphere occurs at temperatures upwards of 2000 K. Consequently, accurate modeling of ionospheric processes requires measurements of reactions at these high temperatures.[1] Also, interest in designing enhanced hypersonic vehicle combustors that employ ion chemistry also necessitates high temperature data to develop similar models.[2,3] Thus, the previously mentioned HTFA apparatus has been designed to address these problems.[4]

The high temperature flowing afterglow (HTFA) operates in the following manner.[4] A heated filament emits energetic electrons that transfer energy to a fast flow of helium buffer gas through collisions that produce electronically excited helium atoms. These excited atoms transfer their energy to a source gas introduced downstream from the filament, whereby the source gas becomes ionized. After tens of centimeters, the ions equilibrate to the flow tube temperature, which is established by heating the tube with a commercially available furnace. A known concentration of reactant gas is introduced and the decrease in the source ion signal is measured. Plotting the decline of the ion signal as a function of reactant concentration over a known reaction time allows the rate constant to be calculated.

Two reactions that have been studied are the charge transfer reactions of Ar^+ with O_2 and CO to produce O_2^+ and CO^+, respectively, as given in Equations (1) and (2).

$$Ar^+\left(^2P_{3/2}\right) + O_2 \rightarrow O_2^+ + Ar \qquad (1)$$

$$Ar^+\left(^2P_{3/2}\right) + CO \rightarrow CO^+ + Ar \qquad (2)$$

The rate constants for both reactions have been previously measured over a wide range of translational energies in a flow drift tube at room temperature by Dotan and Lindinger.[5] The effect of rotational excitation on these reactions has been studied previously in our lab using a variable temperature-selected ion flow drift tube (VT-SIFDT). However, the results are inconclusive.[6] The conditions in the HTFA produce substantial rotational as well as vibrational excitation at the highest temperatures. Therefore, comparing the rate constants measured in the HTFA with the previous drift tube work of Dotan and Lindinger[5] demonstrates the role of internal energy in the charge transfer between Ar^+ with O_2 and CO.[7]

Figure 1 shows the rate constants for reactions (1) and (2) measured in the HTFA plotted against the sum of the average translational and rotational energies. When plotted as such, the HTFA results taken at temperatures up to 900 K agree well with the flow drift tube results of Dotan and Lindinger[5] given by the open symbols. This agreement indicates that rotational and translational energy is equivalent for these reactions. Below 900 K, the rate constants decrease with increasing temperature. The reaction occurs through a collision complex that exists for a few rotational periods such that the energy can be redistributed. If the reaction occurs via multiple passes through an avoided crossing on the potential energy surfaces and the lifetime of the complex decreases with increasing temperature, the complex has less time to access the crossing seam. The transition probability for crossing the seam decreases, in turn decreasing the reaction probability. However, the rate constants increase with increasing temperature above 900 K. The rate constants for reaction from the vibrationally excited states of the O_2 and CO reactants can be calculated, if the total rate constant observed equals the sum of the rate constants from the various vibrational levels weighted by their statistical populations. We also assume that the $v''=0$ and 1 levels both react at the drift tube rate of Dotan and Lindinger[5] and that all vibrational levels above $v''=1$ react at the same rate. The resulting values given in Figure 1 are independent of temperature and are identical to the collision rate constant. This

observation lends supports the argument that the $v''=2$ levels are responsible for the enhancement in the rate constants at high temperatures, which has been observed in other systems as well.[1] Populating this level at higher temperatures makes it energetically allowable under the experimental conditions to produce charge transfer products in an excited electronic state, a process that is quite rapid. Consequently, the rate constants increase when this reaction path becomes available.[5,7]

A similar reaction studied in the HTFA is the charge transfer of Ar^+ with CO_2 shown in Equation 3 that has also been studied in a flow drift tube.[5]

$$Ar^+\left(^2P_{3/2}\right) + CO_2 \rightarrow CO_2^+ + Ar \tag{3}$$

The results for reaction (3) are shown in Figure 2 along with the previous flow drift tube results[5] plotted versus the average total energy, i. e., the sum of the average rotational, translational and vibrational energies. When plotted this way, the results from the two different methods agree well except at the highest few temperatures. The reactivity consequently depends on the total energy available. The rate constants decrease with increasing temperature, again consistent with having a collision complex that lives for a few rotational periods such that the energy can be redistributed. However, at the highest temperatures, the rate constants obtained in the HTFA are lower than those observed in the flow drift tube. If the lifetime of the complex decreases with increasing temperature, the complex may not survive for enough rotational periods at the highest temperatures, thus decreasing the reaction rate. In this case, vibrational excitation hinders the reaction rate, as opposed to reactions (1) and (2) where the excitation enhances it.

A third reaction examined using the HTFA is the charge transfer reaction between O_2^+ and NO which is important in the chemistry of the ionosphere. The reaction, given by Equation (4) is important in maintaining the balance of ionization in the D and E regions from 70 to 150 km in altitude.

$$O_2^+\left(X\ ^2\Pi_g\right) + NO \rightarrow NO^+ + O_2 \tag{4}$$

Because of its role in atmospheric chemistry, the reaction has been studied as a function of kinetic energy using a flow drift tube[8] and as a function of temperature using

a flowing afterglow[9] by Lindinger, et. al. The flowing afterglow study, however, only includes data up to 900 K. The current experiments extend this study to 1400 K using the HTFA apparatus. Figure 3 shows the rate constants obtained in the HTFA plotted versus temperature, along with the earlier flow drift tube[Lindinger, 1974 #478 and flowing afterglow[9] measurements. All of the experiments show that the rate constants are independent of temperature, giving a value that is about half of the collision rate constant. The current results may show a slight increase with increasing temperature at the highest temperatures. Considering the 15% error in the HTFA measurements, the rate constant at 1400 K may be as high as 5.63×10^{-10} cm^3 s^{-1}.

The high temperature flowing afterglow affords the opportunity to study internal energy effects on ion-molecule reaction kinetics. Vibrational excitation increases the reactivity of Ar$^+$ with O_2 and CO but hinders it for Ar$^+$ reacting with CO_2. Only slight vibrational enhancement may arise for O_2^+ charge transfer to NO at ionospheric temperatures. Obtaining empirical values for rate constants at high temperatures is crucial to modelers. Extending the technique to further reactions will provide valuable insight into plasma chemistry.

REFERENCES

[1] P.M. Hierl, I. Dotan, J.V. Seeley, J.M. Van Doren, R.A. Morris, and A.A. Viggiano, J. Chem. Phys. **106**, 3540 (1997).

[2] R. A. Morris, A. A. Viggiano, S. T. Arnold, L. Q. Maurice, and E. A. Sutton, "Reactivity of Air Plasma Ions with Hydrocarbon Fuel Components," presented at the Air Force Office of Scientific Research Molecular Dynamics Contractor's Review, Monterey, CA, 1998 (unpublished).

[3] E. P. Gurijanov and P. T. Harsha, American Institute of Aeronautics and Astronautics , Paper 96 (1996).

[4] P.M. Hierl, J.F. Friedman, T.M. Miller, I. Dotan, M. Mendendez-Barreto, J. Seeley, J.S. Williamson, F. Dale, P. L. Mundis, R.A. Morris, J.F. Paulson, and A.A. Viggiano, Rev. Sci. Inst. **67**, 2142 (1996).

[5] I. Dotan and W. Lindinger, J. Chem. Phys. **76**, 4972 (1982).

[6] I. Dotan and A.A. Viggiano, Chem. Phys. Lett. **209**, 67 (1993).

[7] A. J. Midey and A. A. Viggiano, J. Chem. Phys. , In press (1998).

[8] W. Lindinger, F.C. Fehsenfeld, A.L. Schmeltekopf, and E.E. Ferguson, J. Geophys. Res. **79**, 4753 (1974).

[9] W. Lindinger, D.L. Albritton, F.C. Fehsenfeld, and E.E. Ferguson, J. Geophys. Res. **80**, 3725 (1975).

FIGURES

$$Ar^+ + O_2 \longrightarrow O_2^+ + Ar \qquad Ar^+ + CO \longrightarrow CO^+ + Ar$$

- ●   k CO (HTFA)
- □   k CO (FDT)
- ◆   k O_2 (HTFA)
- △   k O_2 (FDT)
- ▲   k v > 1 CO
- +   k v > 1 O_2

Rate Constant ($cm^3 s^{-1}$)

Translational + Rotational Energy (eV)

Figure 1: Rate constants for the charge transfer reactions of Ar^+ with O_2 and CO plotted against the sum of the average rotational and translational energy. The HTFA points are the present results and the FDT results are the flow drift tube data of Dotan and Lindinger.[5] The rate constants for reaction from the $v''>1$ levels have been calculated using the drift tube results combined with the present results assuming that $v''=0$ and 1of O_2 and CO react at the drift tube rate and all $v''>1$ react at the same rate.
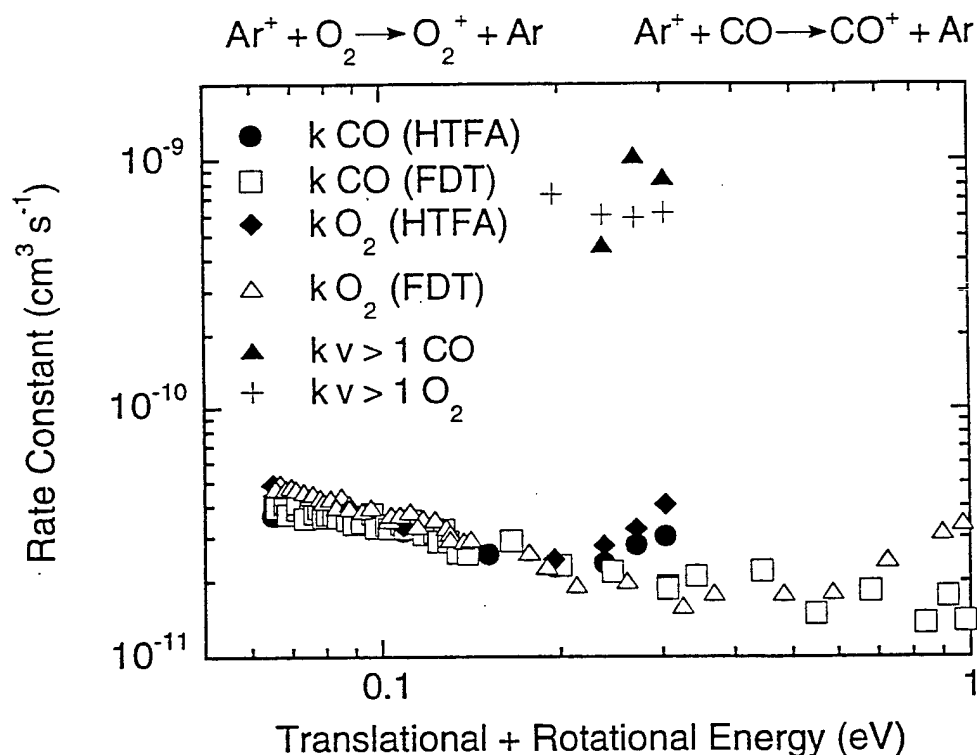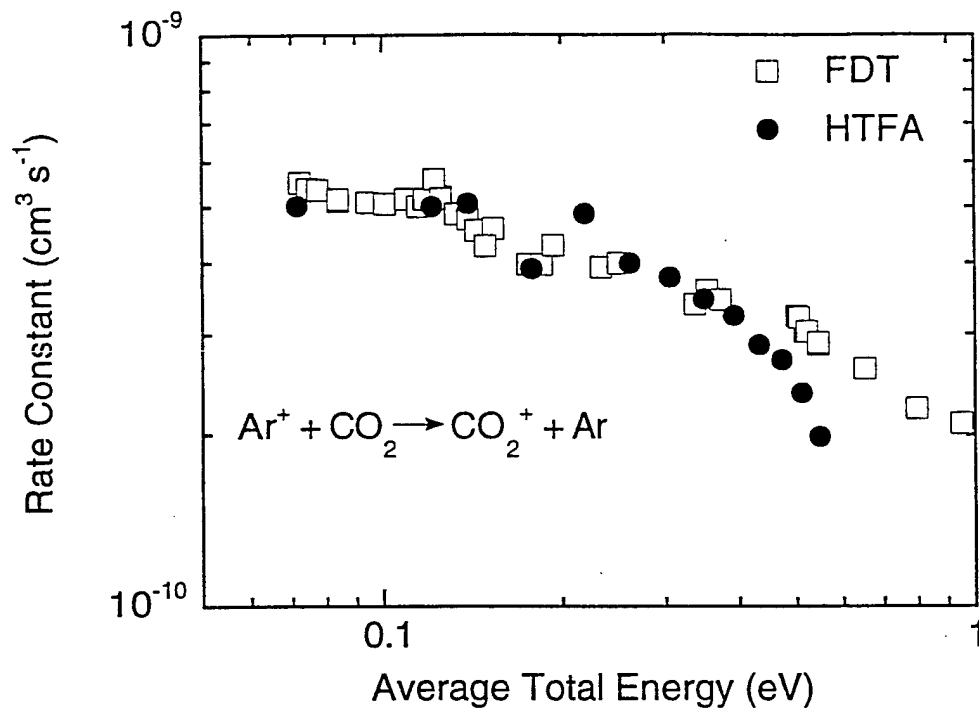
Figure 2: Rate constants for the charge transfer reaction of $Ar^+ + CO_2$ plotted against the sum of the average vibrational, rotational and translational energy. The HTFA points are the present results and the FDT points are the flow drift tube data of Dotan and Lindinger.[5]

$$O_2^+ + NO \rightarrow NO^+ + O_2$$
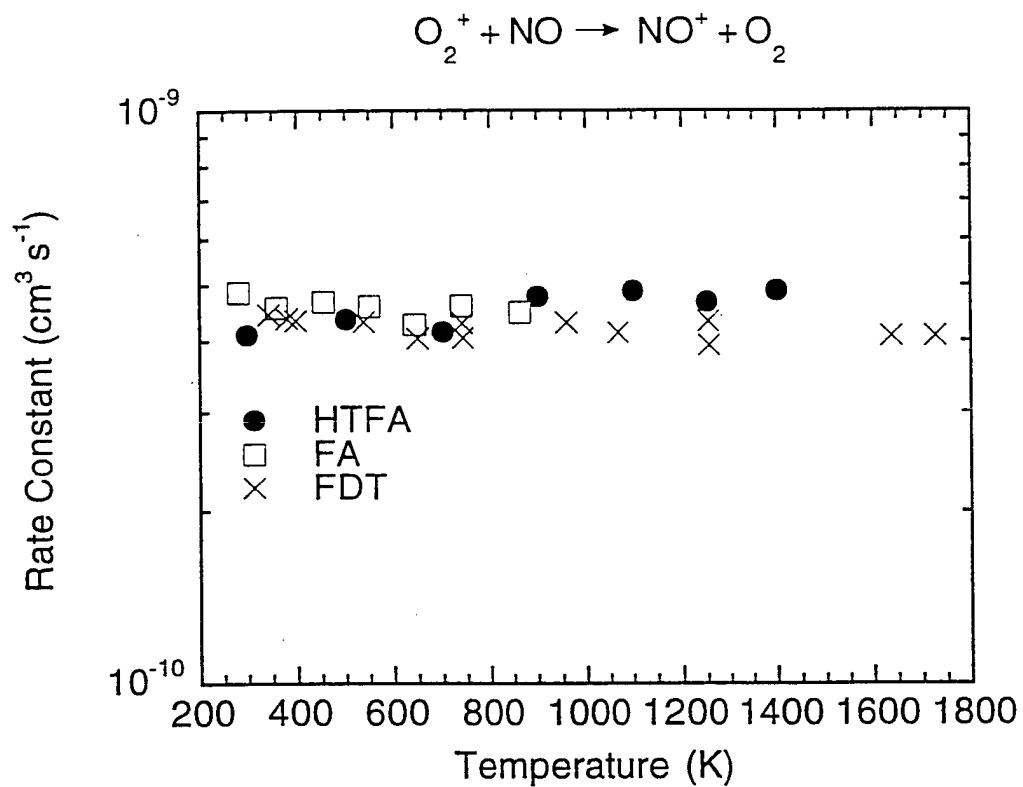
Figure 3: Rate constants for the charge transfer reaction of O2+ + NO plotted against the temperature in K. The HTFA results are the current results and the FDT and FA points are the flow drift tube and flowing afterglow results, respectively, of Lindinger et. al.[8,9]

8

UNITED STATES AIR FORCE

PHILLIPS LABORATORY SCHOLAR PROGRAM

conducted by the

NORTHEAST CONSORTIUM FOR ENGINEERING EDUCATION

FINAL REPORT

Prepared by: Dr. Susan A. Triantafillou.

Research Location: Phillips Laboratory,
                                      Hanscom AFB, MA 01731

Contract Number: F19628-93-C-0027

Susan A. Triantafillou

Contract F19628-93-C-0027

Air Force Research Laboratory / VSBE

29 Randolph Road

Hanscom Air Force Base, Massachusetts 01731-3010

phone: (781) 377-2971,   email: susan@hurricane.plh.af.mil

June 18, 1998

A Lattice Boltzmann Model for Atmospheric Events
Geophysics Scholar Research: March 1997 - May 1998

1   Introduction

This report reviews the work done to adapt the lattice Boltzmann (LB) method to the prediction of atmospheric events, including cloud development and turbulent eddies. These events are relevant to battle site visibility. The scale on which they occur is in between the macrophysical and microphysical scales that are addressed by the currently available specialized models. The LB approach is selected because it parallelizes well and therefore makes large computations feasible.

The LB method has proven useful for numerous fluid dynamics problems. Until recently, the stable applications of the method were confined to isothermal flows. Recent advances [11] have enabled use of the LB approach for problems involving heat transfer without giving up the stability of the isothermal version of the method. It should be noted that while the temperature is allowed to vary, the fluid is still described by an isothermal equation of state. This variable-temperature improvement is used as a basis for additional modifications needed to address the atmospheric problems of interest. The modifications presented in this report address approximating an ideal gas, rather than an isothermal one, and simulating motions in a stratified medium. Experiments with parallelization are also reported here.

This report is organized into sections. Section 2 briefly describes the lattice Boltzmann method and the advances made by other researchers that are relevant to the atmospheric problems of interest. The new modifications proposed by the present study are described in Section 3. Section 4 gives the results and a discussion of the parallelization experiments.

2 The Lattice Boltzmann Method

A brief review of the lattice Boltzmann (LB) method is given here along with a discussion of the relevant improvements and applications. A more detailed presentation of the basic method can be found in [2] or [8]. The improvements and applications discussed here are introduced in [11], [12], and [13].

Perhaps the easiest way to understand the LB method is to consider its historical development. The LB method was preceded by the lattice gas method which uses integers to represent particles that are subject to translations and collisions to simulate a flow. The particles occupy nodes on a regular lattice and are translated along links to neighboring nodes. While this method produces noisy results and some unphysical artifacts, it has the advantages of stability, parallelizability, and a capability to handle complicated boundaries easily. The noise problem is overcome by using real numbers to represent particle distributions and computing collisions according to a Boltzmann equation. In particular, a distribution of particles, $n_a(\mathbf{x}, t)$, located at $\mathbf{x} = (x, y, z)$ at time t and moving in direction a is evolved according to the kinetic equation

$$n_a(\mathbf{x} + \mathbf{e}_a, t + 1) = n_a(\mathbf{x}, t) + \Omega_a(\mathbf{x}, t), \tag{1}$$

where $\mathbf{e}_a$ is a unit vector in direction a and Ω_a is a collision operator for the direction a [6]. The directions are aligned with the links that connect neighboring nodes. The local (number) density, n, and the momentum, $n\mathbf{u}$ are recovered from the distribution by the sums

$$n = \sum_a n_a, \quad n\mathbf{u} = \sum_a n_a \mathbf{e}_a. \tag{2}$$

This technique is called the lattice Boltzmann method. The LB collision operators that were first proposed share some of the problems of the lattice gas method. Namely, these models correspond to a momentum equation that contains an unphysical dependence on density in the advection term and an unphysical dependence of pressure on velocity. These difficulties are resolved by the use of the Bhatnagar, Gross, and Krook (BGK) collision along with a carefully defined equilibrium distribution [8].

The BGK collision can be viewed as a relaxation method in which the collision produces $n_a + \Omega_a = (1 - \omega)n_a + \omega n_a^{eq}$, where ω is the relaxation parameter and n_a^{eq} is the local equilibrium distribution, which is discussed later. The scheme is linearly stable for $0 < \omega < 2$ with $0 < \omega < 1$ resulting in under-relaxation and $1 < \omega < 2$ resulting in over-relaxation. The corresponding kinetic equation is usually written in terms of a relaxation time, $\tau = \frac{1}{\omega}$, as

$$n_a(\mathbf{x} + \mathbf{e}_a, t + 1) = n_a(\mathbf{x}, t) - \frac{1}{\tau}[n_a(\mathbf{x}, t) - n_a^{eq}(\mathbf{x}, t)], \tag{3}$$

and the requirement for linear stabilty is $\tau > \frac{1}{2}$. It will be shown in a subsequent section that the fluid viscosity is proportional to $\tau - \frac{1}{2}$ so that the stability requirement is equivalent to a positive viscosity requirement.

There is some flexibility in the choice of the equilibrium distribution. For example a number of specifications for n_a^{eq} are based on an expansion in powers of the local velocity. The coefficients in a truncated expansion are chosen to get the correct behavior from the model. Typically, the goal is to satisfy the conservation of mass and momentum equations. The unphysical results discussed above can be eliminated by applying certain restrictions to the coefficients in terms of the number of dimensions and the lattice structure. The details of this process are given in Section 2.1 for a particular choice for n_a^{eq}.

It has been demonstrated that n_a^{eq} can be determined so that the LB method simulates continuity, momentum, and energy equations [1] so that flow problems involving heat transfer could be addressed. This approach incorporates stability problems that can be avoided if only the continuity and momentum equations must be satisfied. An alternate approach for addressing heat transfer problems is also available. It relies on a version of the LB method that allows for multiple species, each of which satisfies its own continuity and momentum equations [12]. The different species can interact via interparticle forces and external forces. Heat transfer problems can be handled by letting one of the components represent temperature [11]. This is discussed further in Section 2.2.

2.1   Equilibrium Distribution

This section develops the requirements placed on the coefficients in an equilibrium distribution for a three-dimensional, fourteen-direction model. To do this, a Chapman-Enskog expansion is used to find the differential equations approximated by the lattice Boltzmann equation (with the BGK collision). A particular form for the equilibrium distribution is assumed and examined in terms of the physics it simulates. The complete specification of the equilibrium distribution is given.

The lattice Boltzmann equation in (3) is a discrete version of

$$n_a(\mathbf{x} + \delta_x \mathbf{e}_a, t + \delta_t) - n_a(\mathbf{x}, t) = -\frac{1}{\tau}[n_a(\mathbf{x}, t) - n_a^{eq}(\mathbf{x}, t)], \qquad (4)$$

where the local number density, n, and velocity, $\mathbf{u}$, are found from n_a as shown in (2). A Taylor expansion of n_a can be written

$$n_a(\mathbf{x} + \delta_x \mathbf{e}_a, t + \delta_t) = n_a(\mathbf{x}, t) + \delta_x \mathbf{e}_a \cdot \nabla n_a + \delta_t \frac{\partial}{\partial t} n_a + \frac{1}{2} \delta_x^2 \mathbf{e}_a \mathbf{e}_a : \nabla \nabla n_a n_a$$

3

$$+\delta_x \delta_t \mathbf{e}_a \cdot \nabla \frac{\partial n_a}{\partial t} + \frac{1}{2}\delta_t^2 \frac{\partial^2}{\partial t^2}n_a + \cdots, \tag{5}$$

where everything on the right hand side is evaluated at $(\mathbf{x}, t)$. The Chapman-Enskog approach is used to expand the time derivatives and the distribution function. Multiple time scales are assumed so that,

$$\delta_t \frac{\partial}{\partial t} = \epsilon\frac{\partial}{\partial t_1} + \epsilon^2\frac{\partial}{\partial t_2} + \cdots, \tag{6}$$

where $\epsilon \ll 1$. Changes due to convection are captured by the faster (t_1) time scale, while changes due to diffusion are captured by the slower (t_2) time scale. For near-equilibrium conditions, the distribution, n_a can be expanded as,

$$n_a = n_a^{eq} + \epsilon n_a^{(1)} + \epsilon^2 n_a^{(2)} + \cdots. \tag{7}$$

The lattice Boltzmann equation given by (4) can be rewritten using the Taylor and Chapman-Enskog expansions, which gives the leading order, $O(\epsilon)$, equation

$$\mathbf{e}_a \cdot \nabla n_a^{eq} + \frac{\partial}{\partial t_1}n_a^{eq} = -\frac{1}{\tau}n_a^{(1)} \tag{8}$$

and the next order, $O(\epsilon^2)$, equation

$$\mathbf{e}_a \cdot \nabla n_a^{(1)} + \frac{\partial}{\partial t_1}n_a^{(1)}\frac{\partial}{\partial t_2}n_a^{eq} + \frac{1}{2}\mathbf{e}_a\mathbf{e}_a : \nabla\nabla n_a^{eq} + \mathbf{e}_a \cdot \nabla\frac{\partial}{\partial t_1}n_a^{eq} + \frac{1}{2}\frac{\partial^2}{\partial t_1^2}n_a^{eq} = -\frac{1}{\tau}n_a^{(2)}. \tag{9}$$

The leading order equation can be used to eliminate the higher order derivatives so that

$$\frac{\partial}{\partial t_2}n_a^{eq} + \left(1 - \frac{1}{2\tau}\right)\left(\frac{\partial}{\partial t_1} + \mathbf{e}_a \cdot \nabla\right)n_a^{(1)} = -\frac{1}{\tau}n_a^{(2)}. \tag{10}$$

replaces the $O(\epsilon^2)$ equation given in (9).

The conservation equations are obtained, to order ϵ^2, from Equations (8) and (10). For example, by adding Equation (8) and the product of ϵ and (10), then summing the result over the directions, a, the conservation of mass is obtained to order ϵ^2,

$$\frac{\partial n}{\partial t} + \nabla \cdot (n\mathbf{u}) = 0. \tag{11}$$

The momentum equation is found by adding Equation (8) and the product of ϵ and Equation (10), multiplying the result by $\mathbf{e}_a$ and then summing over a, which can be rearranged to give,

$$\frac{\partial}{\partial t}(n\mathbf{u}) + \nabla \cdot \sum_a \mathbf{e}_a\mathbf{e}_a\left[n_a^{eq} + \epsilon\left(1 - \frac{1}{2\tau}\right)n_a^{(1)}\right] = 0. \tag{12}$$

4

Equation (8) is used to eliminate $n_a^{(1)}$ so that (12) is replaced by

$$\frac{\partial}{\partial t}(n\mathbf{u}) + \nabla \cdot \sum_a \mathbf{e}_a \mathbf{e}_a \left[n_a^{eq} - \epsilon(\tau - \frac{1}{2}) \left(\frac{\partial}{\partial t_1} + \mathbf{e}_a \cdot \nabla \right) n_a^{eq} \right] = 0. \qquad (13)$$

This is further developed for a specific lattice and form for f_a^{eq}.

The form adopted for the equilibrium distribution is the truncated series

$$n_a^{eq} = n(A_a + B_a \mathbf{e}_a \cdot \mathbf{u} + C_a \mathbf{e}_a \mathbf{e}_a : \mathbf{uu} + D_a \mathbf{u} \cdot \mathbf{u}), \qquad (14)$$

for a three-dimensional lattice with $a = 0, \ldots, 14$. Each node is linked to six of its neighbors, in the north, south, east, west, upward, and downward directions, by links of length 1 and to eight of its neighbors in the diagonal directions (for example, the north, east, upward direction) by links of length $\sqrt{3}$. Stationary particles correspond to $a = 0$ with $\mathbf{e}_0 = 0$. It can be assumed that the coefficients A_a, B_a, C_a, and D_a for the fourteen-direction model depend only on $|\mathbf{e}_a|^2$ and the local values for n and $\mathbf{u}$. The requirement, $n = \sum_a n_a^{eq}$, and the summation rules in the Appendix lead to the coefficient constraints

$$A^{(0)} + 6A^{(1)} + 8A^{(3)} = 1, \qquad (15)$$
$$2C^{(1)} + 8C^{(3)} + D^{(0)} + 6D^{(1)} + 8D^{(3)} = 0, \qquad (16)$$

where the superscripts (0), (1), and (3) refer to $|\mathbf{e}_a|^2$ for the given direction. In addition, a distribution that satisfies $n\mathbf{u} = \sum_a n_a^{eq}\mathbf{e}_a$ must have

$$B^{(1)} + 4B^{(3)} = \frac{1}{2}. \qquad (17)$$

The remaining constraints on the coefficients of the equilibrium distribution are found by requiring that the lattice Boltzmann equation is consistent with the momentum conservation equation. The term $\nabla \cdot \sum_a \mathbf{e}_a \mathbf{e}_a n_a^{eq}$, from Equation (12), can be simplified using the summation rules shown in the Appendix to give

$$\nabla \cdot \sum_a \mathbf{e}_a \mathbf{e}_a n_a^{eq} = 2\nabla n[A^{(1)} + 4A^{(4)} + (D^{(1)} + 4D^{(3)} + 4C^{(3)})\mathbf{u} \cdot \mathbf{u}]$$
$$+ 16\nabla \cdot (C^{(3)} n\mathbf{uu}) + 2\nabla(C^{(1)} - 8C^{(3)})n\mathbf{T}, \qquad (18)$$

where

$$\mathbf{T} \equiv \begin{pmatrix} u_x^2 & 0 & 0 \\ 0 & u_y^2 & 0 \\ 0 & 0 & u_z^2 \end{pmatrix}. \qquad (19)$$

This can be further simplified and used to rewrite the $O(1)$ terms in Equation (12) combined with the conservation of mass equation, (11), to obtain ϵ

$$
\begin{aligned}
0 = \ & n\frac{\partial \mathbf{u}}{\partial t} + 16C^{(3)}n\mathbf{u} \cdot \nabla\mathbf{u} + \nabla p + (16C^{(3)} - 1)\mathbf{u}\nabla \cdot (n\mathbf{u}) \\
& + 16n\mathbf{u}(\mathbf{u} \cdot \nabla C^{(3)}) + \nabla \cdot [2n(C^{(1)} - 8C^{(3)})\mathbf{T}] + O(\epsilon),
\end{aligned} \tag{20}
$$

where

$$
p \equiv 2n[A^{(1)} + 4A^{(4)} + (4C^{(3)} + D^{(1)} + 4D^{(3)})\mathbf{u} \cdot \mathbf{u}]. \tag{21}
$$

A comparison of Equation (20) and the Euler equations leads to several more constraints on the coefficients. In order to eliminate the dependence of p on $\mathbf{u}$, the requirement,

$$
4C^{(3)} + D^{(1)} + 4D^{(3)} = 0, \tag{22}
$$

is imposed, which leaves

$$
p = 2n(A^{(1)} + 4A^{(3)}). \tag{23}
$$

The convection term, $n\mathbf{u} \cdot \nabla\mathbf{u}$, has the required coefficient when

$$
C^{(3)} = \frac{1}{16}. \tag{24}
$$

The last term in Equation (20) is eliminated by setting $C^{(1)} - 8C^{(3)} = 0$ so that

$$
C^{(1)} = \frac{1}{2}. \tag{25}
$$

With (22) - (25), Equation (20) becomes

$$
n\frac{\partial \mathbf{u}}{\partial t} + n\mathbf{u} \cdot \nabla\mathbf{u} + \nabla p = O(\epsilon). \tag{26}
$$

The order ϵ terms of Equation (12) are considered in order to obtain the viscous terms in the equation of motion and additional coefficient constraints. Using the form for n_a^{eq} given by (14) and the coefficient constraints given above, these terms are written

$$
\begin{aligned}
\nabla \cdot \sum_a \mathbf{e}_a\mathbf{e}_a(\frac{\partial}{\partial t_1} + \mathbf{e}_a \cdot \nabla)n_a^{eq} = \ & \frac{\partial}{\partial t_1}[\nabla p + \nabla \cdot (n\mathbf{u}\mathbf{u})] \\
& + 16\nabla\nabla \cdot (B^{(3)}n\mathbf{u}) + 8\nabla \cdot \nabla(B^{(3)}n\mathbf{u}) + 2\mathbf{D}[(B^{(1)} - 8B^{(3)})n\mathbf{u}]
\end{aligned} \tag{27}
$$

where

$$
\mathbf{D} \equiv \begin{pmatrix} \partial^2/\partial x^2 & 0 & 0 \\ 0 & \partial^2/\partial y^2 & 0 \\ 0 & 0 & \partial^2/\partial z^2 \end{pmatrix}. \tag{28}
$$

The last term in (27) contributes to the viscosity for certain one-dimensional problems and can be eliminated by setting

$$B^{(1)} - 8B^{(3)} = 0. \tag{29}$$

Together with (17) this gives $B^{(1)} = \frac{1}{3}$ and $B^{(3)} = \frac{1}{24}$. When these coefficients are used in (27), it can be rearranged using the continuity and momentum equations so that to order ϵ

$$-\left(\tau - \frac{1}{2}\right) \nabla \cdot \sum_a \mathbf{e}_a \mathbf{e}_a \left(\frac{\partial}{\partial t_1} + \mathbf{e}_a \cdot \nabla\right) n_a^{eq} = -\eta \nabla^2 (n\mathbf{u}) - \nu \nabla(\nabla \cdot n\mathbf{u}) - \left(\tau - \frac{1}{2}\right) \frac{\partial^2}{\partial t^2} (n\mathbf{u}) \tag{30}$$

where the coefficients of viscosity and bulk viscosity are

$$\nu = \frac{1}{3}\left(\tau - \frac{1}{2}\right) \quad \text{and} \quad \eta = \left[\frac{2}{3} - 2(A^{(1)} + 4A^{(3)})\right]\left(\tau - \frac{1}{2}\right), \tag{31}$$

respectively.

The coefficients $A^{(i)}$ and $D^{(i)}$ are as yet undetermined (as are $B^{(0)}$ and $C^{(0)}$, however these are irrelevant since they are multiplied by $\mathbf{e}_0 = 0$). Two equations for the three $D^{(i)}$ coefficients are provided by (16) and (22). Adopting the choice $D^{(0)} = -\frac{1}{3}$ used by Qian et al. [8] leads to $D^{(1)} = -\frac{1}{6}$ and $D^{(3)} = -\frac{1}{18}$. Furthermore, the choice $A^{(0)} = \frac{2}{9}$ and $\frac{p}{n} = \frac{1}{3}$, also used by Qian et al., implies that $A^{(1)} = \frac{1}{9}$ and $A^{(3)} = \frac{1}{72}$. Note that equating $\frac{p}{n}$ to a constant sets the sound speed to an isothermal one, which in this case has the value $\frac{1}{\sqrt{3}}$.

With these choices for the equilibrium distribution coefficients, the equations of motion in (11) and (13) can be rewritten as the Navier-Stokes equations

$$\frac{\partial \rho}{\partial t} + \nabla \cdot (\rho \mathbf{u}) = 0, \tag{32}$$

$$\rho \frac{\partial \mathbf{u}}{\partial t} + \rho \mathbf{u} \cdot \nabla \mathbf{u} = -\nabla p + \nu \nabla^2 (\rho \mathbf{u}) + \eta \nabla(\nabla \cdot \rho \mathbf{u}), \tag{33}$$

where $\rho = mn$ with m representing the mass per particle and p redefined in terms of ρ (instead of n) so that

$$p = \frac{\rho}{3}. \tag{34}$$

2.2   Passive Scalar Temperature

The use of two species of particles with one representing mass and the other representing temperature was proposed in [11] and is briefly described here. The method is based on the multiple-species method proposed in [12]. Each species, σ, has its

7

own molecular weight, m_σ, density, $\rho_\sigma = m_\sigma n^{(\sigma)}$, and relaxation time, τ_σ. The number density and velocity for each species, $n^{(\sigma)}$ and $\mathbf{u}_\sigma$, respectively, can be computed independently. The two species are assumed to have a common velocity,

$$\mathbf{u}' = \frac{\sum_\sigma \frac{m_\sigma n^{(\sigma)} \mathbf{u}_\sigma}{\tau_\sigma}}{\sum_\sigma \frac{m_\sigma n^{(\sigma)}}{\tau_\sigma}} \tag{35}$$

This common velocity may be incremented by different amounts for each species to reflect accelerations due to the forces associated with each species. In this case, where species 2 is temperature, $m_2 = 0$, $T = n^{(2)}$, the incremented common velocity is the same for both species. In this way, the temperature moves with the fluid as a passive scalar and affects the fluid via a gravtitational force. The result is that species 1 satisfies

$$\frac{\partial \rho}{\partial t} + \nabla \cdot (\rho \mathbf{u}) = 0, \tag{36}$$

$$\frac{\partial \mathbf{u}}{\partial t} + \mathbf{u} \cdot \nabla \mathbf{u} = -\frac{\nabla p}{\rho} + \nu \nabla^2 \mathbf{u} + \mathbf{g}, \tag{37}$$

where $\rho = m_1 n^{(1)}$ and species 2 satisfies

$$\frac{\partial T}{\partial t} + \mathbf{u} \cdot \nabla T = k \nabla^2 T, \tag{38}$$

where $k = \frac{1}{3}(\tau_2 - \frac{1}{2})$.

2.3   A Note on Computer Implementation

The methods described above are programmed using FORTRAN 90 and computed sequentially. Parallelization is discussed later. The code is tested using several problems with known solutions. For example, the single-species code is checked by running a 'viscometer' problem and an acoustics problem. The viscometer test problem, proposed in [5] uses the decay of a Poiseuille flow to measure the viscosity. This two-dimensional problem is run in several orientations for several values of τ to confirm that the code is running properly.

Additional tests are done using a one-dimensional acoustics problem. The small-disturbance assumption of acoustics is made so that the Navier-Stokes equations can be linearized using the expansions

$$\rho(\mathbf{x}, t) = \rho_0(\mathbf{x}) + \epsilon \rho_1(\mathbf{x}, t) + \cdots, \tag{39}$$

$$p(\mathbf{x}, t) = p_0(\mathbf{x}) + \epsilon p_1(\mathbf{x}, t) + \cdots, \tag{40}$$

$$\mathbf{u}(\mathbf{x}, t) = \mathbf{u}_0(\mathbf{x}) + \epsilon \mathbf{u}_1(\mathbf{x}, t) + \cdots, \tag{41}$$

where the subscript 0 refers to the undisturbed state, the subscript 1 is the leading order approximation of the disturbance, and $\epsilon \ll 1$. These expansions, along with the assumption of isentropic flow lead to the following one-dimensional approximation for ρ_1

$$\frac{\partial^2 \rho_1}{\partial t} - \frac{p_0}{\rho_0}\frac{\partial^2 \rho_1}{\partial x^2} - (\nu + \eta)\frac{\partial^2}{\partial x^2}\frac{\partial \rho_1}{\partial t} = 0, \qquad (42)$$

where ν and η are the viscosity and the kinematic viscosity, respectively. The periodic solution has the form,

$$\rho_1 = Ae^{at}\cos(bt + \phi)\sin\left(\frac{2\pi k}{L}x\right), \qquad (43)$$

where L is the length of the domain, ϕ is a phase angle, A and k are constants determined by the initial conditions and

$$a = -2(\nu + \eta)\left(\frac{\pi k}{L}\right)^2, \qquad (44)$$

$$b = \pm\left(\frac{2\pi k}{L}\right)\sqrt{\frac{p_0}{\rho_0} - (\nu + \eta)^2\left(\frac{\pi k}{L}\right)^2}, \qquad (45)$$

so that $\frac{p_0}{\rho_0}$ and $\nu + \eta$ can be found from (44) and (45).

The accuracy of the lattice Boltzmann solution to the one-dimensional acoustics problem can be assessed by applying the method for given values of A, k, and L and measuring the error in $\frac{p_0}{\rho_0}$ (the square of the sound speed) and $\nu + \eta$. The phase angle ϕ is also found in the process, although it does not play a part in evaluating the lattice Boltzmann solution. The values of a, b, and ϕ for the lattice Boltzmann solution are taken to be those that minimize the error in ρ_1 defined by

$$E(a, b, \phi) = \sum_{t_j}\sum_{x_i}[\rho_1(a, b, \phi; x_i, t_j) - \rho_1^{LB}(x_i, t_j)]^2, \qquad (46)$$

where $\rho_1(a, b, \phi; x_i, t_j)$ is calculated using (43) and $\rho_1^{LB}(x_i, t_j)$ is a lattice Boltzmann result. The minimum value for E corresponds to

$$\mathbf{F} \equiv \left(\frac{\partial E}{\partial a}, \frac{\partial E}{\partial b}, \frac{\partial E}{\partial \phi}\right) = 0. \qquad (47)$$

The solution (a, b, ϕ) can be found using a numerical root-finding method.

This problem is used to test the lattice Boltzmann code for lattices with 20, 40, 60, and 80 nodes in the x-direction over a 40 time-step period. The values $k = 2$ and $\tau = .7$ are used and L is set to the number of nodes in the x-direction. Equation (47) is solved using a combination of steepest descents, to get a rough approximation,

9

and Newton's method, to get a more accurate solution. The results for a and b are used to obtain the observed values for $\frac{p_0}{\rho_0}$ and $\nu + \eta$ to be compared to theoretical values determined by the lattice and the equilibrium distribution as discussed in Section 2.1. The errors in the soundspeed values decreased quadratically with lattice size and ranged from .1% (for the 80-node lattice) to 1.2% (for the 20-node lattice). The smaller-order effects due to viscosity are not predicted with quadratic accuracy, however the maximum error is only 1%.

3 Special Applications and Extensions of the lattice Boltzmann Method

Several modifications and adaptations of the lattice Boltzmann method have been developed in working towards a model suitable for predicting atmospheric events that involve moist air. The first topic addressed here, numerical boundary conditions, is relevant to a wide range of problems in fluid dynamics. Next, modeling stratification, an important feature of the atmosphere, is discussed. Stratification can be achieved in the lattice Boltzmann model by applying the appropriate external forces. This is explored below with an example of a gravity wave problem. Finally, there is a proposed modification to the lattice Boltzmann method for simulating flow of an ideal, rather than an isothermal, gas.

3.1 Boundary Conditions

Numerical boundary conditions must be applied outside of the domain, at the boundary nodes, so that during streaming, the appropriate distributions are streamed into the domain. This must be done so that the lattice Boltzmann equation is satisfied at the boundary. If this requirement is ignored in assigning distributions at the boundaries, then it is effectively like using different values of τ at these sites. The result would be a nonuniform and incorrect viscosity field. Dirichlet and no-slip boundary conditions are addressed here. The method described below is adapted from [11] for general boundary shapes.

For this discussion, it is assumed that the initial condition assigns $n_a = 0$ for any node outside the domain of the flow. Thus, after streaming, nodes adjacent to the interior of the domain, or boundary nodes, have nonzero distributions directed away from the domain. These directions are denoted $a(-)$. The distributions directed into the domain, or in the $a(+)$ directions, are specified as discussed below. The distributions that neither direct particles into or out of the domain have directions

$a(0)$. These are unspecified and will remain that way since they are not required for computation purposes.

The Dirichlet condition in a D-dimensional domain specifies the number density, n, and the velocity, $\mathbf{u}$, at each boundary node, placing $1 + D$ restrictions on the values assigned to $n_{a(+)}$ and $n_{a(0)}$. For example, consider a three-dimensional, fourteen-direction model applied to a case with a horizontal boundary. The Dirichlet condition introduces only four equations, to evaluate ten unknowns. A simple way of imposing additional requirements for a general boundary shape follows.

Conservation of mass and momentum are satisfied when the collision operator, $-1/\tau(n_a - n_a^{eq})$ is applied. Summing over all directions, the collision results in

$$-\frac{1}{\tau}\left(\sum_{a(+)}(n_a - n_a^{eq}) + \sum_{a(-)}(n_a - n_a^{eq}) + \sum_{a(0)}(n_a - n_a^{eq})\right) = 0. \qquad (48)$$

The $a(0)$-direction distributions can be assigned (somewhat arbitrarily) so that,

$$\sum_{a(0)} n_a = \sum_{a(0)} n_a^{eq}. \qquad (49)$$

A choice for $n_{a(+)}$ that satisfies (48) is

$$n_{a(+)} = -n_{a(-)} + n_{a(-)}^{eq} + n_{a(+)}^{eq}, \qquad (50)$$

in which $\mathbf{e}_{a(+)}$ and $\mathbf{e}_{a(-)}$ have opposite directions. Once this assignment is made for all links directed into the domain, the collision calculation can be carried out for those links using the given density and velocity at the boundary. Note that the approach can be applied to any boundary node, regardless of boundary orientation or shape. An alternative to selecting $\mathbf{e}_{a(-)}$ so that it is opposite $\mathbf{e}_{a(+)}$ is to make the selection based on a reflection. The reflection rule would not work for certain irregular boundaries, since it is possible to reflect particles with an $a(-)$ direction and obtain a new $a(-)$ direction rather than an $a(+)$ direction.

A boundary condition that specifies $\mathbf{u}$ but not n corresponds to a no-slip boundary. This can be implemented using a similar approach. A difference is that in the no-slip case some symmetry is assumed and the distributions, $n_{a(+)}$, are assigned using $n_{a(-)}$ according to a reflection or a bounce-back (opposite) rule. Therefore, in addition to Equations (48) and (49), the condition $\sum_{a(-)} n_a = \sum_{a(+)} n_a$ along with $\mathbf{u} = 0$ gives

$$n = \frac{2\sum_{a(+)} n_a}{\sum_{a(+)} A_a + \sum_{a(-)} A_a}. \qquad (51)$$

The collision is then computed using n as given in Equation (51) and $\mathbf{u} = 0$ to determine $n_{a(+)}^{eq}$ and using the reflected or bounced value for $n_{a(+)}$ (as the prior-to-collision value).

3.2 Gravity Waves and the Relevant External Forces

A medium which has as its steady state a uniform density and a potential temperature that varies exponentially with height is discussed here. These conditions are relevant to the problem of gravity waves in a shallow volume. The external forces required to maintain the desired stratified flow are presented below. Following that is an outline of a gravity-wave problem along with computational results.

3.2.1 External Forces

External forces are incorporated into the multiple-species model to simulate the effects of gravity based on the approach in [13]. This leads to a general form of the mass balance equation for each species. Each species, σ, is acted upon by its own external force, $\mathbf{F}_\sigma = n^{(\sigma)} m_\sigma \mathbf{g}_\sigma$, where $n^{(\sigma)}$ and m_σ are the number density and mass per particle, respectively of species σ and $\mathbf{g}_\sigma$ is the acceleration due to the force on species σ. The model also allows for interparticle forces and a distinct equilibrium distribution function for each species, however, these capabilities are not used here.

The present application requires a two-species model, where species 1 represents the density, $\rho = m_1 n^{(1)}$, of a fluid and species 2 represents its potential temperature, $\theta = n^{(2)}$. The molecular weights are $m_1 = 1$, $m_2 = 0$. The external force $\mathbf{F}_1$ is a direct simulation of $\rho \mathbf{g}$, where $\mathbf{g}$ is the acceleration due to gravity. The force $\mathbf{F}_2$ acts to maintain the exponential variation of species 2 with height. The forces are specified in accordance with the mass balance equation from [13]. For species 1 this leads to the required conservation equation, regardless of the values assigned to $\mathbf{g}_1$ and $\mathbf{g}_2$. For species 2 this leads to

$$\frac{\partial n^{(2)}}{\partial t} + \nabla \cdot (n^{(2)} \mathbf{u}) = \nabla \cdot \left(-\mathcal{D}_1 \frac{n^{(2)}}{n^{(1)}} \nabla n^{(1)} + \mathcal{D}_2 \nabla n^{(2)} + \tau_2 n^{(2)} (\mathbf{g}_1 - \mathbf{g}_2) \right), \quad (52)$$

where $\mathcal{D}_\sigma$ is proportional to $(\tau_\sigma - \frac{1}{2})$. The assignment of $\mathbf{g}_1$ is discussed first, then $\mathbf{g}_2$ is found to satisfy (52).

The density used in the calculation, $\mathbf{F}_1 = \rho \mathbf{g}$, is approximated using a Boussinesq assumption as discussed in [11]. It is redeveloped here for the case where species 2 is the potential temperature (rather than the temperature). To establish how the density varies with the other variables, consider the potential temperature in the form

$$\theta = \kappa \frac{p^{1/\gamma}}{\rho}, \quad (53)$$

where γ is the ratio of specific heats and κ is a constant. This is rewritten with

12

following expansions

$$\theta = \theta_0(z) + \theta_1(x, y, z, t) + \cdots, \tag{54}$$

$$p = p_0(z) + p_1(x, y, z, t) + \cdots, \tag{55}$$

$$\rho = \rho_0 + \rho_1(x, y, z, t) + \cdots, \tag{56}$$

where θ_1/θ_0, p_1/p_0, and ρ_1/ρ_0 are at least an order of magnitude smaller than one (though not necessarily comparable in order to one another). Substituting the expansions into (53) leads to

$$\frac{\theta_1}{\theta_0} = \frac{1}{\gamma} \frac{p_1}{p_0} - \frac{\rho_1}{\rho_0}, \tag{57}$$

neglecting higher order terms. Changes in density are primarily due to changes in potential temperature so that

$$\frac{\rho_1}{\rho_0} \approx -\frac{\theta_1}{\theta_0} \tag{58}$$

and the density can be written

$$\rho \approx \rho_0 \left(1 - \frac{\theta_1}{\theta_0}\right). \tag{59}$$

In the static, conductive state the vertical momentum equation becomes

$$-\nabla p + \rho \mathbf{g} = 0. \tag{60}$$

This can be rewritten using (59) as $-\nabla p^* + \rho_0 \theta_1/\theta_0 \mathbf{g} = 0$, where p^* has been substituted for $p + \rho_0 g z$ with $g = |\mathbf{g}|$. Eliminating the unknown, θ_1, gives

$$\mathbf{F}_1 = -\rho_0 \left(\frac{\theta - \theta_0}{\theta_0}\right) \mathbf{g} = \rho_0 \left(\frac{\theta - \theta_0}{\theta_0}\right) g \mathbf{e}_k = n^{(1)} m_1 \mathbf{g}_1 \tag{61}$$

so

$$\mathbf{g}_1 \approx \frac{\theta - \theta_0}{\theta_0} g \mathbf{e}_k. \tag{62}$$

The value of $\mathbf{g}_2$ is chosen to get the required variation of species 2 with height in static equilibrium. Species 2 varies according to

$$n^{(2)} = \theta_0(0) \exp\left(\frac{kz}{g}\right), \tag{63}$$

where $\theta_0(0)$ and k are constants. This state is maintained by making the following assignments

$$\tau \equiv \tau_1 = \tau_2, \tag{64}$$

$$\mathcal{D} \equiv \mathcal{D}_1 = \mathcal{D}_2, \tag{65}$$

$$\mathbf{g}_2 = \mathbf{g}_1 + \frac{\mathcal{D}k}{g\tau} \mathbf{e}_k, \tag{66}$$

13

where where $\mathcal{D} = \frac{1}{3}(\tau - \frac{1}{2})$ and $\mathbf{e}_k$ is the unit vector in the positive, vertical direction. Note that if species 2 were uniform or varied linearly, (52) would reduce to the required conservation of mass equation provided that $g_1 = g_2$.

In practice F_1 and F_2 are applied to both species because species 2 is a passive scalar and its velocity is equal to the velocity of species 1. The forces are applied by incrementing the (common) velocity according to

$$\mathbf{u} \leftarrow \mathbf{u} + \tau \left(\frac{\theta - \theta_0}{\theta_0} g + \frac{\mathcal{D}k}{g\tau} \right) \mathbf{e}_k. \tag{67}$$

The equations of motion are

$$\frac{\partial \rho}{\partial t} + \nabla \cdot (\rho \mathbf{u}) = 0, \tag{68}$$

$$\frac{\partial \mathbf{u}}{\partial t} + \mathbf{u} \cdot \nabla \mathbf{u} = -\frac{\nabla p}{\rho} + \nu \nabla^2 \mathbf{u} + \mathbf{g}, \tag{69}$$

$$\frac{\partial \theta}{\partial t} + \mathbf{u} \cdot \nabla \theta = \nu \nabla^2 \theta. \tag{70}$$

These look like Equations (36) − (38), except here the density of species 2, is the potential temperature, θ, and the thermal conductivity is equal in value to the viscosity due to the requirement $\tau_1 = \tau_2$.

3.2.2 A Gravity-Wave Problem

A gravity-wave problem is done to illustrate the use of the forces described above. More details on this and related problems are given in [4], [7], and [9]. Gravity waves, or buoyancy waves, cause mountain lee waves and clear air turbulence and are important in atmospheric modeling.

For the simple gravity-wave problem considered here, the equations of motion can be approximated so that an exact solution is found. In keeping with the Boussinesq approximation used to obtain external forces, the atmosphere is assumed to be incompressible, so that conservation of mass becomes

$$\nabla \cdot \mathbf{u} = 0. \tag{71}$$

For inviscid motions the momentum equations are

$$\frac{\partial \mathbf{u}}{\partial t} + \mathbf{u} \cdot \nabla \mathbf{u} = -\frac{\nabla p}{\rho} + \mathbf{g} \tag{72}$$

and in the absence of thermal conductivity the potential temperature is governed by

$$\frac{\partial \theta}{\partial t} + \mathbf{u} \cdot \nabla \theta = 0. \tag{73}$$

14

These equations are linearized for small motions relative to the overall height of the atmosphere. This corresponds to small changes in the measured physical quantities and a large Froude number,

$$Fr = \frac{U}{NH} \gg 1, \tag{74}$$

where U is the characteristic velocity, N is the characteristic buoyancy frequency (discussed later), and H is the characteristic vertical displacement of air. A two-dimensional problem is considered and the physical quantities are expanded as in (54) - (56) with the velocity $\mathbf{u} = (u, w)$ expanded as

$$u = u_0 + u_1(x, z, t) + \cdots, \tag{75}$$

$$w = w_1(x, z, t) + \cdots, \tag{76}$$

where the leading order quantities have the subscript 0 and the corrections, which are an order of magnitude smaller have the subscript 1. Note u_0 is constant. Using the expansions, Equation (72) gives the leading order vertical momentum equation as the static equilibrium condition

$$\frac{dp_0}{dz} = -\rho_0 g, \tag{77}$$

where $g = |\mathbf{g}|$, so that $p_0(z) = p_0(0) - \rho_0 g z$. The next order momentum equations are

$$\left(\frac{\partial}{\partial t} + u_0 \frac{\partial}{\partial x}\right) u_1 + \frac{1}{\rho_0} \frac{\partial p_1}{\partial x} = 0, \tag{78}$$

$$\left(\frac{\partial}{\partial t} + u_0 \frac{\partial}{\partial x}\right) w_1 + \frac{1}{\rho_0} \frac{\partial p_1}{\partial z} - \frac{\theta_1}{\theta_0} g = 0, \tag{79}$$

where Equation (58) has been used to replace ρ_1 in the gravity term. The continuity equation, (71), is approximated as

$$\frac{\partial u_1}{\partial x} + \frac{\partial w_1}{\partial z} = 0 \tag{80}$$

and the potential temperature equation (73) becomes

$$\left(\frac{\partial}{\partial t} + u_0 \frac{\partial}{\partial x}\right) \theta_1 + w_1 \frac{d\theta_0}{dz} = 0. \tag{81}$$

These equations can be rearranged to obtain a single equation with one unknown. This is done by taking a z derivative of the x-momentum equation and an x derivative of the z-momentum equation and combining the results to eliminate pressure. This gives

$$\left(\frac{\partial}{\partial t} + u_0 \frac{\partial}{\partial x}\right) \left(\frac{\partial u_1}{\partial z} - \frac{\partial w_1}{\partial x}\right) + \frac{g}{\theta_0} \frac{\partial \theta_1}{\partial x} = 0. \tag{82}$$

The operator $\frac{\partial}{\partial x}\left(\frac{\partial}{\partial t} + u_0 \frac{\partial}{\partial x}\right)$ is applied to this result. The the term $\frac{\partial^2 u_1}{\partial x \partial z}$ can be replaced using the continuity equation given by (80) and the term $\left(\frac{\partial}{\partial t} + u_0 \frac{\partial}{\partial x}\right)\theta_1$ can be replaced using Equation (81). The final result is

$$\left(\frac{\partial}{\partial t} + u_0 \frac{\partial}{\partial x}\right)^2 \left(\frac{\partial^2 w_1}{\partial x^2} + \frac{\partial^2 w_1}{\partial z^2}\right) + N^2 \frac{\partial^2 w_1}{\partial x^2} = 0, \tag{83}$$

where

$$N^2 = g\frac{d(\ln\theta_0)}{dz}, \tag{84}$$

the square of the buoyancy frequency, is assumed to be constant. Equation (83) has wave solutions of the form

$$w_1 = We^{i\phi}, \quad W = W_r + iW_i, \quad \phi = kx + mz - vt \tag{85}$$

where k and m are wave numbers and v is a frequency. A dispersion relation,

$$(k^2 + m^2)(v - u_0 k)^2 - N^2 k^2 = 0 \tag{86}$$

is found by substituting the solution (85) into (83).

The streamline at the surface provides further information about the values of k and m. Once w_1 is found, Equations (59) and (77) - (80) can immediately be solved to give

$$\rho = \frac{-\rho_0 N^2 w_1 i}{g(v - u_0 k)}, \tag{87}$$

$$u = u_0 - \frac{m}{k}w_1, \tag{88}$$

$$\theta = \theta_0(0)\left(1 + \frac{N^2 w_1 i}{g(v - u_0 k)}\right)\exp\left(\frac{N^2 z}{g}\right), \tag{89}$$

$$p = p_0(0) - \rho_0 g z + \rho_0 \frac{m}{k^2}(v - u_0 k)w_1. \tag{90}$$

The real parts of Equations (85) and (87) - (90) correspond to the physical solutions.

Consider steady gravity waves (so $\phi = kx + mz$) due to a corrugated topography where the elevation varies like $\cos\phi$. Provided that $mz \ll kx$ on the surface, the shape of the mountain determines k and using (86) the value of m is given by

$$m^2 = \frac{N^2}{u_0^2} - k^2. \tag{91}$$

If m is real, then there is no decay with height. An example of such a solution is shown in Figure 1. The figure shows constant-θ lines, or streamlines, of the flow past a section of a corrugated surface containing a single mountain. The relevant constants
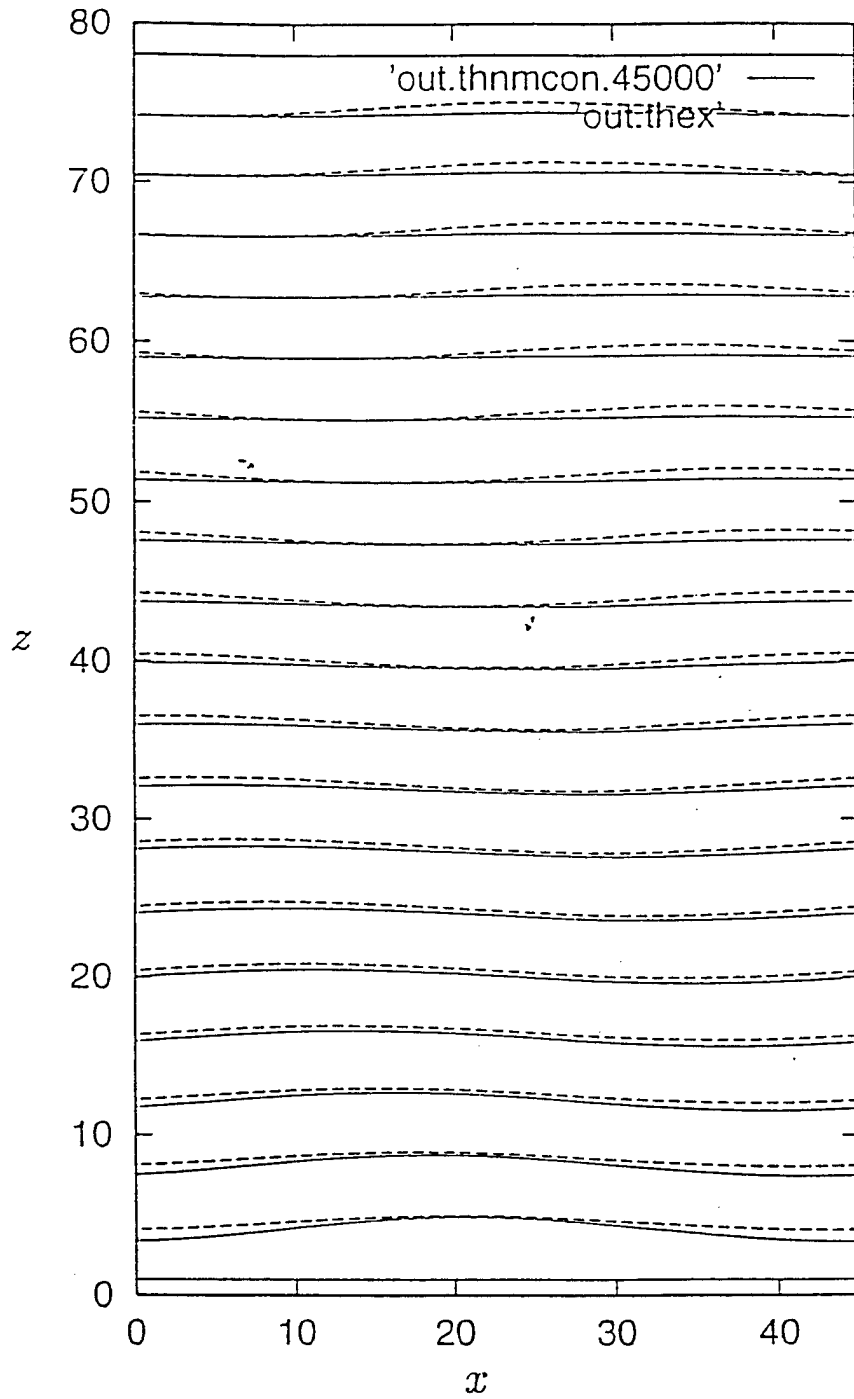
16

Figure 1: Streamlines for flow past a corrugated surface. The solid lines show the results of a lattice Boltzmann computation; the dashed lines represent the exact solution to the approximate gravity-wave problem.

are $k = \frac{\pi}{23}$, $m = .08$, $N^2 = 2 \times 10^{-6}$, $u_0 = .00893$, $W_r = 0$, $W_i = -.000551$. The solid lines show the lattice Boltzmann result after 45,000 time steps. The initial condition is undisturbed flow (with $\rho = \rho_0$, $u = u_0$, $w = 0$, $\theta(z) = \theta_0(z)$) and the boundary conditions are Dirichlet (as discussed in Section 3.1) at the bottom, Neumann at the top, and periodic on the sides. The values $\tau = .52$ and $g = .003$ are also used. The dashed lines show the solution according to Equation (89). Causes of discrepancies include the use of a viscous, nonlinear model for an inviscid, linear problem. The viscosity in the numerical solution is $\nu = .00667$ and the degree to which the problem is nonlinear correlates to the Froude number.

In order to get the Froude number for this example, the characteristic vertical displacement must be written in terms of the known quantities so that Equation (74) can be applied. The change in height of the fluid moving along the streamline given by the mountain surface is $\int w(x, \mathcal{H}(x)) dt$ where the surface is given by $z = \mathcal{H}(x)$. For a corrugation with period $\frac{2\pi}{k}$, the time required for fluid to move from the lowest to the highest point is about $\frac{\pi}{k\hat{u}}$, where $\hat{u}$ is a characteristic horizontal velocity. Letting $\hat{w}$ be the characteristic vertical velocity, the characteristic verticle displacement of air is

$$H = \frac{2\hat{w}}{k\hat{u}}. \tag{92}$$

For the example of Figure 1 $\hat{u}$ and $\hat{w}$ may be taken to be u_0 and $|W|$, respectively, so the Froude number is $Fr = 7.0$. Recall that the linear solution is valid for $Fr \gg 1$.

Additional experiments with gravity-wave problems could be done. With the problem discussed above the solution could be computed for increasingly finer grids to check that the 'more accurate' solutions approach the solution to the linear problem. Alternatively, the solution could be computed for increasingly greater Froude numbers to confirm that the agreement between the linear solution and the LB solution improves as the linear approximation gets closer to the full solution. A more realistic lower boundary condition could be used so that the fluid is subject to a no-slip condition along a mountain (defined in terms of lattice nodes). Nonlinear gravity-wave problems can also be solved.

3.3 A Modified Equation of State

The lattice Boltzmann method simulates a fluid with an isothermal sound speed. While the passive scalar temperature method allows changes in temperature to affect the external forces on the fluid, the pressure remains a constant multiple of the density. The value of the constant is determined by the constants chosen for the coefficients,

$A^{(1)}$ and $A^{(3)}$ in the equilibrium distribution. A more general approach to selecting $A^{(1)}$ and $A^{(3)}$ is to let

$$h(\mathbf{x}, t) \equiv \frac{p}{n}. \tag{93}$$

With $A^{(0)} = \frac{2}{9}$ the remaining coefficients are

$$A^{(1)} = \frac{1}{4}\left(\frac{7}{9} - h\right) \quad \text{and} \quad A^{(3)} = \frac{1}{16}\left(-\frac{7}{9} + 3h\right). \tag{94}$$

Particle distributions should be positive. A conservative requirement that assures this is $A^{(1)}, A^{(3)} > 0$. This leads to the condition

$$\frac{7}{27} < h < \frac{7}{9}. \tag{95}$$

To simulate ideal-gas behavior, h is made proportional to the temperature,

$$h = RT, \tag{96}$$

where the constant R can be taken to be the molecular weight multiplied by the specific gas constant.

Several test runs were made to experiment with the use of nonuniform and variable h. In the two tests described below small pressure jumps move through a medium. Gravity and viscosity can be neglected and the acoustic approximation is made, so that the disturbances travel at the soundspeed. The situation can be modeled by the integral conservation equations, simplified to reflect the assumptions listed above. The results of this model are compared to the results of the LB model.

The first test simulates two uniform media, such as air and water, separated by a boundary surface. Each medium has its own density, ρ_1 or ρ_2. The media are at rest and the pressure, p_0, is uniform so that the boundary remains at rest and the value of h is different in the different media. An acoustic disturbance, with pressure p_d and speed u_d, is initiated away from the boundary and then passes through one medium and into the second. When the disturbance reaches the boundary, a reflected wave is returned and a transmitted wave propagates into the second medium. The behavior of the wave is determined by the acoustic impedance in each medium, $\mathcal{R}_i = \rho_i c_i$, where c_i is the soundspeed in medium i. The difference between the final pressure and the undisturbed pressure is $2(p_d - p_0)\mathcal{R}_2/(\mathcal{R}_1 + \mathcal{R}_2)$. The computations, using the lattice Boltzmann code for a case in which the densities of the two media initially differ by about a factor of two, gives results for density that are within 3% of the expected values.

A second test involves a left-traveling pressure jump and a right-traveling pressure jump in a single medium. The pressure jumps are small enough (less than 5%) to be

considered using an acoustic approximation and p/ρ is nearly constant. Therefore, this test problem could also be done using a lattice Boltzmann model based on a fixed value of h. Each moving pressure jump causes an initially uniform state to jump to a new state. The two jumps collide and form a new state and two new jumps as shown in Figure 2. The pressure in the new state is within .3% of the value given by the integral conservation equations. While this does not demonstrate a new capability of the lattice Boltzmann method, it does show a successful approximation using the variable h model.

It is important to note that the method described does not conserve energy. A simple example illustrates the difference in behavior of an energy-conserving fluid and a fluid that obeys the LB model with variable h. If two equal volumes of stationary fluid with differing densities, pressures, and temperatures are allowed to mix, then when equilibrium is reached, the fluid is stationary and has a new uniform state. Conservation of mass requires that the new density be the average of the two original densities. Conservation of energy for a perfect gas requires that the new temperature be a mass-weighted average of the original temperatures. The lattice Boltzmann method with h set according to the perfect gas law will correctly predict the final density, but will incorrectly predict the final temperature as the average of the original temperatures.

4 Parallelization

The efficiency of the lattice Boltzmann (LB) method is realized when the computations are done using parallel processing. The opportunity to parallelize the LB code was used to investigate a new programming language called ZPL. It is a machine-independent, array language developed at the University of Washington in Seattle, Washington. An advantage of ZPL is that a single program can be compiled for different single- or multiple-processor machines by using a machine-specific compiler designed to exploit the target computer. Upon compilation the ZPL code produces C code, which is then compiled by the local C compiler. When a ZPL program is compiled for sequential computations the performance of the code is comparable to that of a C program written for a single processor. A drawback to ZPL is that it is new and still under development so that certain features are not yet available and presumably the chances of discovering a bug are greater for ZPL than for a more established compiler.

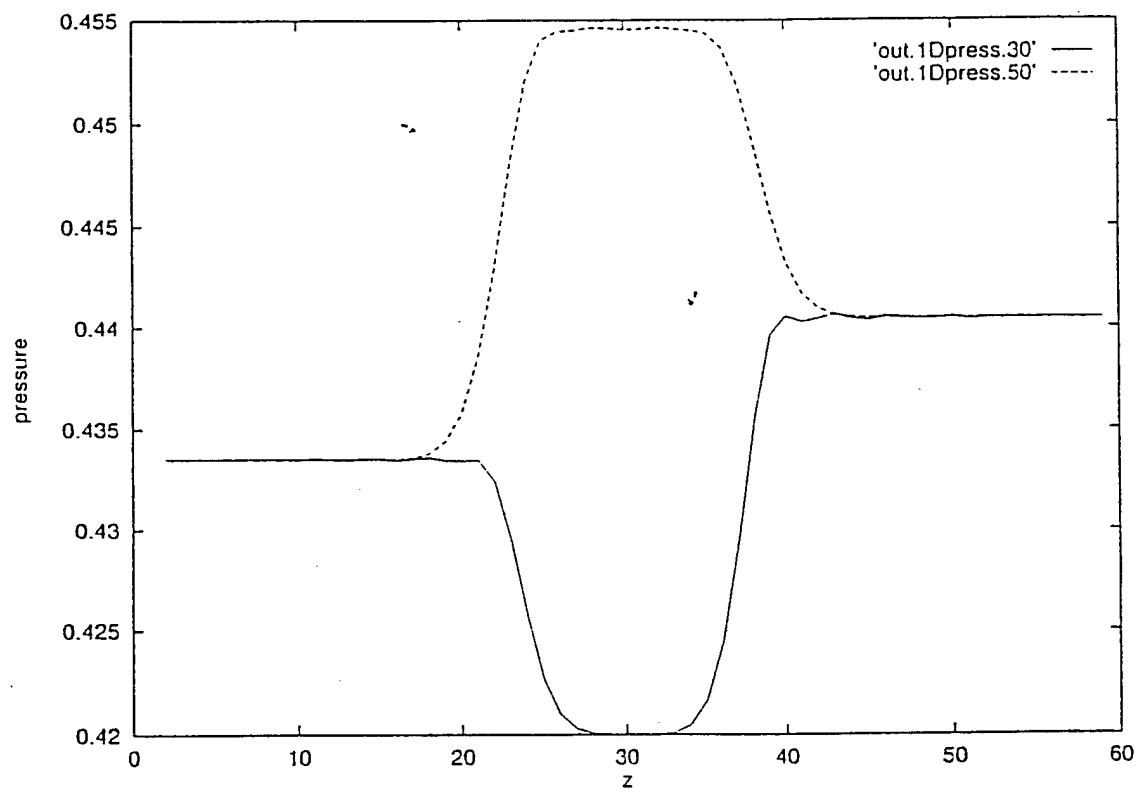To experiment with ZPL the basic LB method is coded using ZPL and the pro-

Figure 2: Moving pressure jumps. The solid curve shows two pressure jumps (traveling towards the center) before they collide, at time=30, the dashed curve shows the new pressure jumps at time=50 (traveling away from the center) produced by the collision.

gram is compiled and run on different machines. The program solves the viscometer problem on a $10 \times 10 \times 10$ grid over 500 time steps (so that a total of 5×10^5 individual LB computations are done). The first machine used is an SGI Origin 200, a two-processor, 180 megahertz machine. When the code is compiled and run sequentially the run time required is 1:56 (given as minutes:seconds). The run time for the same computation done in parallel is 1:01. A more detailed look at the run times shows that the speed-up is primarily due to parallelizing the collision computations which approximately halves the collision computation time from 1:54 to 0:58. The time used for streaming is nearly the same for both approaches (the times are 0:03 for sequential and 0:04 for parallel computations). This is as expected since it is the collision calculations that require only local information and therefore lend themselves to parallelization. The results also demonstrate that most of the compute time is accounted for by the collisions.

The second machine used to try the ZPL program is an SGI Onyx, a four-processor, 200 megahertz machine. The very same code that worked on the Origin gave incorrect results on the Onyx. Experiments with several simpler test codes and many exchanges with the ZPL support group at the University of Washington point to a bug in the ZPL compiler for the Onyx. While the specific problem has not been identified, the ZPL support group is willing to work on it given a short program that isolates the problem. Producing such a code and resolving the problem would be called for if ZPL use is to be continued. This matter is being considered. In summary, when ZPL works correctly, it performs as advertised, but its reliability is questionable.

5 Conclusion

The modifications proposed by the present study are elements of an atmospheric event simulator. In addition to the extensions suggested in the previous sections, additional modifications are called for in order to simulate cloud-forming processes. In particlular vapor and liquid water can be incorporated as two additional model components. As flow conditions change, mass may be transferred from one component to the other to reflect phase changes. Phase transitions can be specified using the cloud parameterization method used in the Penn State/NCAR Mesoscale Model (MM5) [3].

6 Appendix

Useful sums from [10] for evaluating terms in LBE model with on a fourteen-direction lattice, where the links have lengths 1 and $\sqrt{3}$,

$$E_{ij}^{(2)} = \sum_a w(|\mathbf{e}_a|^2)e_{ai}e_{aj} \tag{97}$$

$$= 2[w(1) + 4w(3)]\delta_{ij} \tag{98}$$

$$E_{ijkl}^{(4)} = \sum_a w(|\mathbf{e}_a|^2)e_{ai}e_{aj}e_{ak}e_{al} \tag{99}$$

$$= 8w(3)\Delta^{(4)} + 2[w(1) - 8w(3)]\delta^{(4)} \tag{100}$$

where

$$\Delta^{(4)} = \delta_{ij}\delta_{kl} + \delta_{ik}\delta_{jl} + \delta_{il}\delta_{jk}, \tag{101}$$

$$\delta^{(4)} = +\delta_{ij}\delta_{kl}\delta_{ik}, \tag{102}$$

and the subscripts (i, j, k, l) refer to the coordinate directions and w is a function of the length of link a.

References

[1] Alexander, F. J., S. Chen, and J. D. Sterling, Lattice Boltzmann thermohydrodynamics, *Phys. Rev. E*, **47** 4 (1993) pp. R2249 - R2252.

[2] Chen, H., S. Chen, and W. H. Mattheus, Recovery of the Navier-Stokes equations using a lattice-Boltzmann method, *Phys. Rev. E*, **45** 8 (1992) pp. R5339 - R5342.

[3] Grell, G. A., J. Dudhia, and D. R. Stauffer **A Description of Fifth-Generation Penn State/NCAR Mesoscale Model (MM5)**, NCAR/TN-398+STR, National Center for Atmospheric Research, Boulder, CO, (1994).

[4] Holton, J. R., **An Introduction to Dynamic Meteorlogy**, Academic Press, Boston, (1992).

[5] Kadanoff, L. P, G. R. McNamara, and G. Zanetti, A Poiseuille viscometer for lattice gas automata, *Lattice Gas Methods for Partial Differential Equations*, edited by B. D. Doolan et al., Addison-Wesley Publishing Co., New York, (1990).

[6] McNamara, G. R. and G. Zanetti, Use of the Boltzmann equation to simulate lattice-gas automata, *Phys. Rev. Lett.*, **61** 20 (1988) pp. 2332 -2335.

[7] Pedlosky, J., **Geophysical Fluid Dynamics**, Springer-Verlag, New York, (1987).

[8] Qian, Y. H., D. d'Humières, and P. Lallemand, Latttice BGK models for Navier-Stokes equation, *Europhys. Lett.*, **17**, 479 (1992) pp. 479 - 484.

[9] Queney, P., The problem of air flow over mountains: A summary of theoretical studies, *Bulletin of the American Meteorological Society*, **29**, Jan (1948) pp. 16 - 25.

[10] Wolfram, S., Cellular automaton fluids 1: Basic theory, *Lattice Gas Methods for Partial Differential Equations*, edited by B. D. Doolan et al., Addison-Wesley Publishing Co., New York, (1990).

[11] Shan, X., Simulation of Rayleigh-Bénard convection using a lattice Boltzmann method, *Phys. Rev. E*, **55** 3, (1997), pp. 2780 - 2788.

[12] Shan X. and G. Doolen, Multicomponent lattice-Boltzmann model with inter-particle interaction, *J. Statistical Phys.* **81** 1/2 (1995), pp 379 - 393.

[13] Shan X. and G. Doolen, Diffusion in a multicomponent lattice Boltzmann equation model, *Phys. Rev. E*, **54** 4, (1996), pp. 3614 - 3620.